Astronomy & Astrophysics manuscript no. aanda
December 15, 2025

MIRACLE

III. JWST/MIRI expose the hidden role of the AGN outflow in NGC 1068

C. Marconcini[1,2], A. Marconi[1,2], M. Ceci[1,2], A. Feltre[2], M. Tartėnas[3], K. Zubovas[3], I. Lamperti[1,2], G. Cresci[2], L. Ulivi[2,4], F. Mannucci[2], E. Bertola[2], C. Bracci[1,2], E. Cataldi[1,2], Q. D'Amato[2], J.A. Fernández-Ontiveros[5], J. Fritz[6], E. Hatziminaoglou[7,8,9], I. E. López[10], M. Ginolfi[1,2], C. Gruppioni[10], M. Mingozzi[11], B. Moreschini[1,2], G. Sabatini[2], F. Salvestrini[12,13], M. Scialpi[1,2], G. Tozzi[14], A. Vidal-García[15], C. Vignali[10,16], G. Venturi[17,2], and M.V. Zanchettin[2]

(Affiliations can be found after the references)

Received —; accepted —

ABSTRACT

We present new JWST Integral Field Spectroscopy (IFS) observations of the type-II active galaxy NGC 1068. We combined Mid-InfraRed (Mid-IR) and optical IFS data from MIRI and MUSE to characterize the multi-phase circumnuclear gas properties and its interaction with the AGN outflow and radio jet. MIRI data trace the ionized and molecular gas emission up to $\sim$ 400 pc from the nucleus at 20–60 pc spatial resolution, unveiling a clumpy ionized structure surrounding the radio hot-spots and a rotating warm molecular disc. We exploited innovative Mid-IR diagnostic diagrams to highlight the role of the AGN as the main excitation source for the ionized gas across the entire MIRI field of view, consistent with optical diagnostics, and supporting the scenario of an AGN-driven wind. Density sensitive [Ne V] and [Ar V] Mid-IR transitions reveal compact high-density clumps ($n_e \geq 10^4$ cm^{-3}) along the edges of the jet and outflow, likely tracing gas compression by the expanding wind. We combined multi-cloud kinematic (MOKA^{3D}) and photo-ionization (HOMERUN) modeling to characterize the ionized outflow properties. We find that [O IV] traces an outflow $\sim$300 km s^{-1} faster than that inferred from [O III], demonstrating that the two lines originate from distinct gas components. This kinematic dichotomy is independently confirmed by the photoionization analysis, which requires a dust-poor, unextinguished component dominating the optical lines and a dust-rich, extincted component responsible for the Mid-IR high-ionization emission, including [O IV]. The Mid-IR–revealed dusty component carries a significantly larger ionized-gas mass than what can be inferred from optical lines alone, showing that most of the outflowing mass is hidden from classical optical diagnostics. Kinematic and photoionization models consistently point to a two-stage acceleration scenario, with velocities reaching $\sim$2000 km s^{-1}, consistent with an energy-driven wind. Our multi-cloud modelling indicates that the outflow entrains up to a few 10^6 M$_\odot$ of ionized gas and couples efficiently with the surrounding ISM, injecting substantial turbulence and strongly impacting the host-galaxy environment.

Key words. galaxies: Seyfert - galaxies: ISM - galaxies: active - ISM: kinematics and dynamics - ISM: jets and outflows

1. Introduction

Active Galactic Nuclei (AGN) are expected to play a pivotal role in shaping the evolution processes of the host galaxy through various feedback mechanisms (e.g., Fabian 2012; Kormendy & Ho 2013). The energy released by accretion of matter onto the central supermassive black holes (SMBHs) can sustain powerful winds that propagate through the host galaxy, impacting the surrounding interstellar medium (ISM), and possibly enhancing or quenching star formation by compressing, heating, or sweeping the ambient gas (e.g., King & Pounds 2015; Marconcini et al. 2025b). The role of AGN-driven outflows is now routinely included in theoretical models and hydrodynamical simulations of galaxy evolution to explain the observed galaxy properties and the scaling relations that hold between host galaxies and their central SMBHs (e.g., Di Matteo et al. 2005; Fabian 2012).

In recent years, theoretical predictions and observations have provided compelling evidence and underscored the necessity for a comprehensive, multi-phase investigation of AGN-driven outflows. This investigation aims to fully constrain the impact of the wind on its host and gain a broader understanding of the mechanism driving the wind (e.g., Cicone et al. 2014; King & Pounds 2015; Fiore et al. 2017; Ward et al. 2024). Various gas phases can be driven outwards by the wind, contributing to the total budget of outflowing gas mass and to the energy injected into the surroundings. Ionized outflows are mainly traced by strong optical emission lines such as [O III]λ5007 and Hα, and can reach maximum velocities of up to a few 10^3 km s^{-1}, pushing the ionized gas up to kpc scales (e.g. Carniani et al. 2015; Fiore et al. 2017; Venturi et al. 2018, 2021; Cresci et al. 2023; Marconcini et al. 2025b). Cold and warm molecular outflows (T $\sim$ 10–100 K) are routinely traced by CO and H_2 transitions, respectively, in the millimeter and InfraRed (IR) bands, and are found to be slower compared to the ionized counterpart, reaching velocities of $\sim 10^2$ km s^{-1}. Nonetheless, molecular gas winds are observed to carry a substantial amount of mass ($M_{out} \sim 10^7$-10^9 M$_\odot$) and thus are expected to play a key role in regulating the star formation and the host gas content (Carniani et al. 2015; Fluetsch et al. 2019; Riffel et al. 2023).

AGN are also known to accelerate high-velocity jets, which can heat the gas in the host halo, preventing its accretion onto the SMBH and strangulating star formation. Moreover, powerful jets are observed and predicted to drag and heat large amounts of gas along their path, inject turbulence, possibly regulating the gas kinematic on kiloparsec scales and contributing to the gas acceleration (Pillepich et al. 2018; Mukherjee et al. 2018b; Venturi et al. 2021; Cresci et al. 2023; Audibert et al. 2023).

The JWST/MIRI Medium Resolution Spectrometer (MRS; Rieke et al. 2015; Wells et al. 2015; Labiano et al. 2021) already started to revolutionize our knowledge of the mid infrared (Mid-

IR) emission originating from the circumnuclear region of local AGN, resolving the emission of the ionized and warm molecular gas phases. In particular, warm molecular transitions trace gas cooling from a warm shocked medium, and are thus enhanced in outflowing environments. Additionally, the Mid-IR regime is characterized by lower extinction with respect to shorter wavelengths, allowing for a comprehensive investigation of the obscured outflow properties down to a few tens of pc close to the SMBH (Zhang et al. 2024; Ramos Almeida et al. 2025; Esparza-Arredondo et al. 2025; Marconcini et al. 2025a; Hermosa Muñoz et al. 2025; Ceci et al. 2025; López et al. 2025).

Estimating the physical properties of multi-phase outflows, such as their mass outflow rates, momentum, and energy, is pivotal to constrain their impact on galactic scales and feedback models (Harrison et al. 2018; Harrison & Ramos Almeida 2024). Specifically, it is crucial to estimate the amount of gas dragged by the wind and escaping the galaxy potential, the link between the accretion and ejection rates which regulates the interplay between the SMBH and the host, and finally the energetic coupling efficiency with the ISM, that ultimately defines the role of the outflow in driving the galaxy evolution processes. Nevertheless, despite their importance, the determination of outflow physical properties with current methodologies suffer of large systematic uncertainties (e.g. Cicone et al. 2018; Veilleux et al. 2020). As a result, a robust comparison with theoretical models and numerical simulations remains challenging.

In this paper, we present a detailed analysis of the multiphase gas properties in the circumnuclear region of the local Seyfert II galaxy NGC 1068. We focused on new JWST Cycle 3 data from our Mid-IR Radiation Activity of Cicumnuclear Line Emission program (MIRACLE; Marconcini et al. 2025a; Ceci et al. 2025), aided by archival optical and millimeter data from the Multi Unit Spectroscopic Explorer (MUSE; Bacon et al. 2010) and the Atacama Large Millimeter Array (ALMA; Wootten & Thompson 2009), respectively.

This paper is organized as follows: In Section 2, we summarize the observations and data analysis procedures for MIRI, MUSE, and ALMA. In Section 3 we present the results and a detailed morphological, kinematic and ionization analysis of the multi-phase gas properties across different scales, exploiting Mid-IR and optical tracers as well as kinematics and photoionization models. We also discuss the implications of our findings in the context of AGN feedback and multi-phase gas outflows. Finally, in Section 4 we summarize our results. In all the maps presented in this paper the north is up and east is to the left.

2. Observations and data analysis

2.1. NGC 1068

NGC 1068 is a barred, spiral galaxy which, despite being classified as a radio-quiet source, is among the brightest Seyfert galaxies in the radio regime with L(10 MHz-100 GHz) = 3.6×10^{40} erg s^{-1} (Wilson & Ulvestad 1983). NGC 1068 hosts a SMBH of 0.8-1.7 $\times$ 10^7 M$_\odot$ (Lodato & Bertin 2003; Impellizzeri et al. 2019) and a low-power radio jet (P = 2 $\times$ 10^{43} erg s^{-1} Mutie et al. 2024) directed northeast-southwest (see Fig. 1 and Gallimore et al. 1996; Capetti et al. 1997; Mutie et al. 2024). Such low-power jets are observed to play a role in heating the kpc-scale ISM and affect the gas kinematics within the inner hundreds of parsecs (see e.g. López et al. 2025). Optical and mm analysis reveal that the radio-jet is co-spatial with the AGN ionization bi-cone, which is inclined by $\sim 5^\circ$ with respect to the plane of the sky (Cecil et al. 1990; Das et al. 2006; Barbosa et al. 2014; May & Steiner 2017) and by $\sim 45^\circ$ with respect to the galactic disc (Bland-Hawthorn et al. 1997; García-Burillo et al. 2014). To characterize the multi-phase gas properties in the circumnuclear region of NGC 1068 (D = 14.2 Mpc, Bland-Hawthorn et al. 1997, $1'' \sim 68$ pc) we focused on the recently acquired JWST/MIRI data and archival VLT/MUSE and ALMA observations. A comprehensive description of the data reduction is presented in the Appendix A.

2.2. JWST/MIRI, VLT/MUSE and ALMA data

JWST data were acquired with MIRI in MRS mode, as part of the MIRACLE program (ID 6138, P.I C. Marconcini & A. Feltre) on 2024 December 27 UT using a single pointing. We used the MRS with all four integral-field units available (channels 1-4), covering the spectral range 4.9-28.1 μm, with three grating settings, SHORT (A), MEDIUM (B), and LONG (C) for each channel. For each sub-channel we adopted a five groups and 30 integrations observing strategy, with a four-pointing dither pattern. For an overview of the MIRI/MRS data reduction procedure see Appendix A.1 and Marconcini et al. (2025a). NGC 1068 archival Integral Field Spectroscopy (IFS) data obtained with MUSE (ID: 094.B-0321, P.I. A. Marconi) were obtained as part of the "Measuring AGN Under MUSE" (MAGNUM) program (Cresci et al. 2015; Venturi et al. 2018; Mingozzi et al. 2019; Marconcini et al. 2023, 2025b). To investigate the cold molecular gas phase in NGC 1068 we analyzed archival ALMA 12-m band 6 observations (ID: 2016.1.00232.S, P.I. S.Garcia-Burillo) covering the observed spectral window of [226.91, 228.79] GHz which allowed us to trace the CO (2-1) emission at 230.538 GHz rest-frame. The ALMA Field of View (FoV) is 38$''$ in diameter, with a largest recoverable scale of 11.4$''$ (780 pc) and a 19 pc spatial resolution (beam size FWHM 0.33$''$ $\times$ 0.37$''$).

Figure 1 shows the FoVs of the various instruments, as well as the ionized gas emission at different scales and wavelengths. In particular, Fig. 1 (left) shows the ionized emission traced by [O III]λ5007 from MUSE, with the ALMA and MIRI FoVs overlaid. The right panel shows the [OIV]26μm emission from MIRI, with VLA[1] 14.9 GHz radio contours, tracing the well-known radio jet in NGC 1068. Figure 2 shows the rest-frame MIRI/MRS integrated spectrum extracted from the green circular region shown in Fig. 1, selected as the closest region to the AGN with co-spatial outflow and bow-shock signatures. Spectral features from different MRS bands compared along this work are based on a stitched spectrum computed following the strategy presented in Ceci et al. (2025). Such a strategy is crucial when comparing features of different MIRI bands as it accounts for the flux conservation in each band and for the different pixel size of each channel. In particular, we re-binned the emission of each channel to the coarser pixel size of channel 4 (hereafter Ch4) and multiplied the spectra by a tailored scaling factor to align the spectra of adjacent bands. As shown in Fig. 2, we detected more than 20 ionized gas transitions, and seven H_2 pure-rotational transitions, from H_2 S(7) to H_2 S(1). Table D.1 lists the flux and uncertainty of all the detected emission lines extracted from the largest recoverable area that covers all the MIRI/MRS wavelength range (i.e. the FoV of Ch1). In Sect. 3.4.3, we will use these fluxes to model the gas physical properties. Interestingly, as shown by Fig. 2, we found weak evidence of polycyclic aromatic hydrocarbons (PAHs) emission only at 6.2μm in the extracted spectrum and overall in the entire MIRI FoV. This is

[1] We downloaded VLA calibrated images from the NRAO archive https://www.vla.nrao.edu/astro/nvas/.

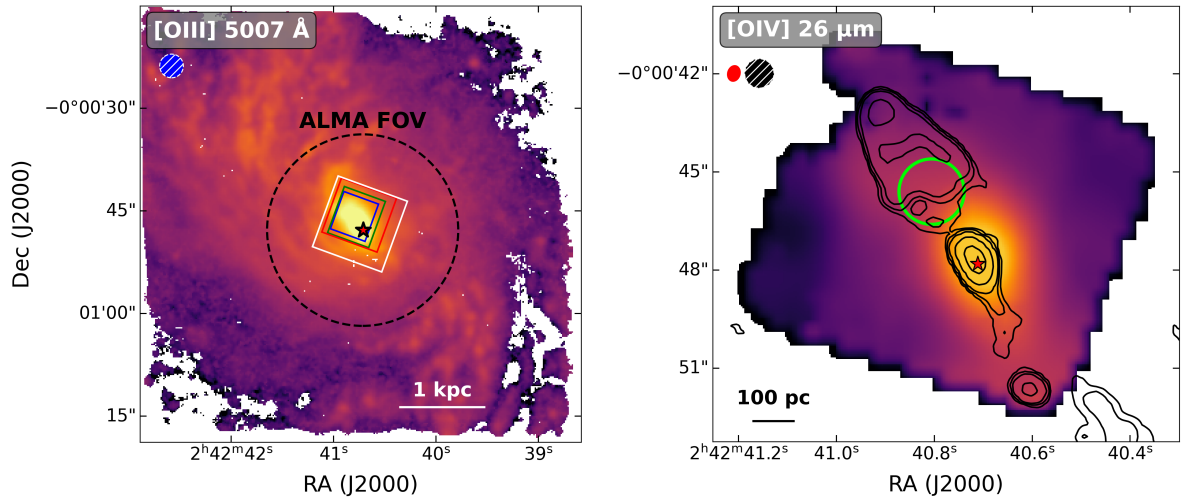

Fig. 1. NGC 1068 emission line images obtained from MIRI and MUSE data-cubes. Left: MUSE WFM [O III]λ5007 emission line map. The ALMA FoV is shown as a dashed black circle. The FoVs of the four MIRI MRS channels are shown, from Ch1 to Ch4, in blue, green, red, and white, respectively. The blue circle represent the MUSE beam. Right: MIRI Ch4 [O IV]$\lambda 26\mu m$ emission line map with VLA 14.9 GHz (U-band) radio emission drawn at levels of [9, 15, 27, 120, 600] times the rms (73.1 μJy). The red star marks the AGN position identified by X-ray imaging (Marin et al. 2024). The green circle represent the $1''$ extraction region of the MIR spectrum shown in Fig. 2. Red and black circles represent the VLA and MIRI beams, respectively.

possibly due to UV dissociation by the AGN radiation, X-ray disruption, or to the intense AGN continuum emission which can hide faint features (Jensen et al. 2017; Monfredini et al. 2019). Moreover, since our MIRI observations cover a limited area centered on the luminous AGN ionization cone and co-spatial with the radio jet, it is likely that fast shocks caused by the jet impacting onto the ISM suppress PAH structures (see e.g. Micelotta et al. 2010). Finally, Fig. 2 shows mild evidence of the ∼5.8–6.2 μm water ice absorption band, that forms by the freezing of water vapor onto dust grains and suggests the presence of cold and dense clouds in an obscured environment (Spoon et al. 2022; García-Bernete et al. 2024). The physical properties of PAHs and water ice in the MIRACLE sample will be addressed in a forthcoming paper.

To analyze the emission line properties both in the Mid-IR, optical, and (sub)mm regimes we adopted a tailored spectroscopic routine presented in App. B. The goal of this analysis is to fit the continuum and emission lines on a spaxel-by-spaxel basis adopting multiple Gaussian components, when needed to reproduce complex line profiles. In the following, in case of a multi-Gaussian fit, we considered the Gaussian component with lower width to be representative of the systemic, ordered kinematics and the broader components to trace the disturbed motions, likely tracing outflowing gas.

3. Results and discussion

As a result of the spaxel-by-spaxel emission line fitting procedure (see App. B), we obtain the total best-fit model for each emission line. In this section we exploit the flux estimates of Mid-IR and optical emission lines to investigate the physical and kinematical properties of the ionized gas in NGC 1068.

3.1. Multiphase gas kinematics

Figure 3 shows the integrated flux maps, the line of sight (LOS) velocity and velocity dispersion maps for the [O III]λ5007, [NeV]14μm, [OIV]26μm (hereafter [O III], [Ne V], and [O IV], respectively), $H_2S(1)$, and CO (2-1) emission from MUSE, MIRI, and ALMA datacubes.

We observe that the [O III]λ5007, [Ne V], and [O IV] transitions share similar flux morphology and kinematics, suggesting a common origin and likely powering source, despite their different ionization potentials (IP) of 35eV, 97eV, and 55eV, respectively. The flux maps of these transitions show that the northeast-southwest ionization bi-cone illuminated by the AGN is co-spatial to the well-known radio-jet (Mutie et al. 2024) and warm ionized outflow (Kakkad et al. 2018; Mingozzi et al. 2019; Venturi et al. 2021). Such a configuration might be indicative of a tight interaction between the ionized outflow and the jet (Capetti et al. 1997; May & Steiner 2017). Moreover, the LOS velocity and velocity dispersion maps of these transitions share extremely peculiar features. First, the LOS velocity maps show multiple gradients of the gas velocity along the jet direction, alternating blueshifted and redshifted peaks of emission both in the northeast and the southwest cones, which lie above and below the galactic disc, respectively (see e.g., Crenshaw & Kraemer 2000; Das et al. 2006; Müller-Sánchez et al. 2011; Barbosa et al. 2014; Venturi et al. 2021). Second, the velocity dispersion maps of the ionized gas show a clear enhancement perpendicular to the ionization cones and radio-jet (for a detailed discussion on this feature in the ionized phase in NGC 1068, see Venturi et al. 2021). This feature has been detected in many local Seyfert galaxies, both in the ionized (Feruglio et al. 2020; Venturi et al. 2021; Girdhar et al. 2022; Ulivi et al. 2024), warm molecular (Riffel et al. 2015), cold molecular (Shimizu et al. 2019), and all of these phases simultaneously (Marconcini et al. 2025a). The most credited scenario proposed to explain this phenomenon is that while the jet, and to a lesser extent the outflow, impacts the galaxy disc, it induces high turbulence in the ambient material, as supported by cosmological and hydrodynamic simulations (Pillepich et al. 2018; Mukherjee et al. 2016, 2018b; Meenakshi et al. 2022). Bottom panels in Fig. 3 show the moment maps of the warm and cold molecular phases, traced by the $H_2S(1)$ and CO (2-1) emission, respectively. Interestingly, the molecular phase shows a more diffuse gas distribution with respect to the ionized phase. The flux map of the CO (2-1) emission highlights the well known

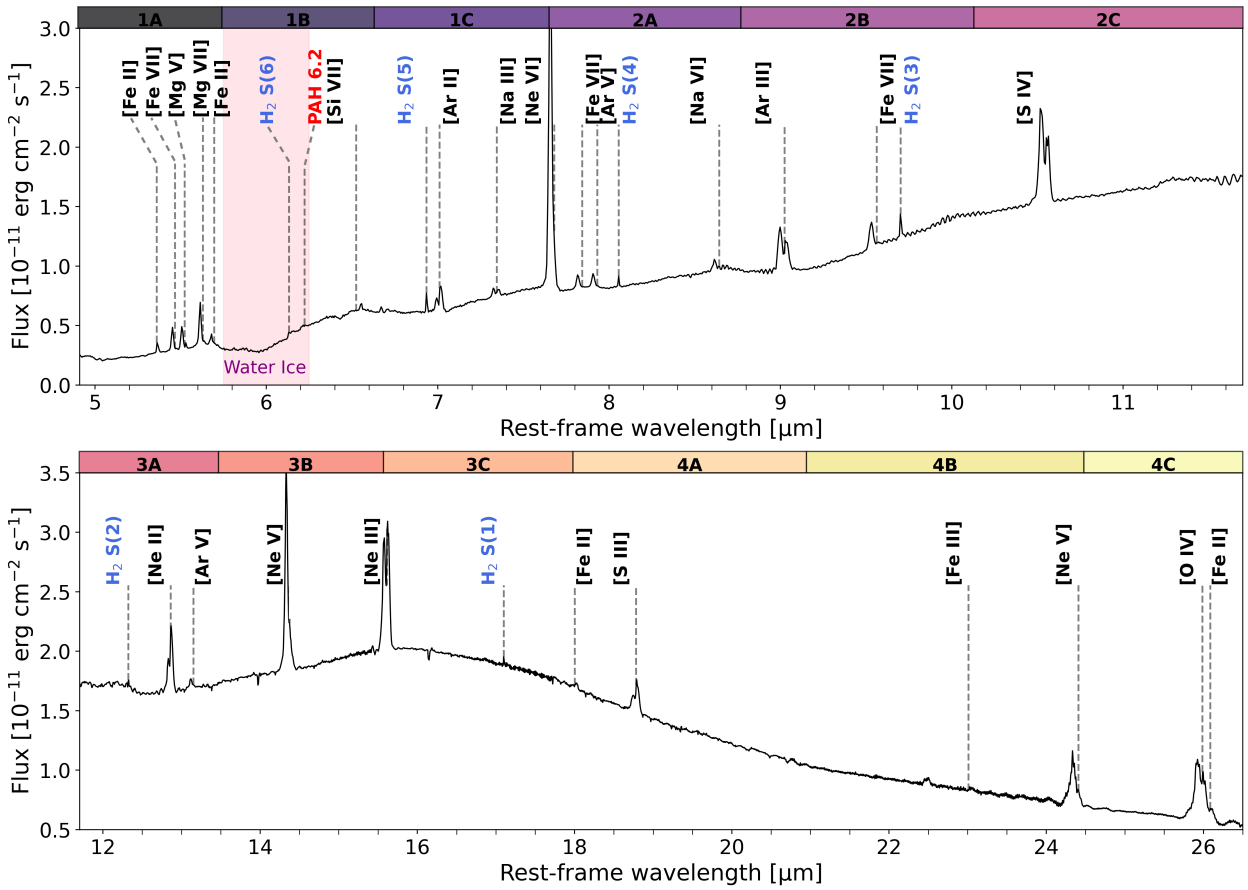

Fig. 2. MIRI MRS rest-frame integrated spectrum of NGC 1068 extracted from the green circular aperture of radius 1″ shown in Fig. 1 with spectral features marked. All the emission lines detected in the integrated spectrum are highlighted. The $H_2S(7)$ transition at 5.5 μm is not labeled for visualization purposes as it is blended with the [Mg V]. The spectral range of the various MIRI MRS channels and bands are shown as colored rectangles on top of the spectra. The water ice 5.8-6.2 μm band is shown in shaded purple.

300 pc circumnuclear molecular disc (CND) (Schinnerer et al. 2000; García-Burillo et al. 2014) offset from the AGN position. Moreover, we observe that both the warm and cold molecular gas tracers show a cavity around the AGN, possibly due to the ionized outflow which is destroying the molecular gas (García-Burillo et al. 2014, 2019). To support this scenario, we extracted an integrated spectrum from a circular aperture centered on the nucleus and with radius of 0.4″ and confirmed the non detection of any of the eight pure-rotational warm molecular transitions. Despite both molecular tracers show evidence of a purely rotating pattern (see Fig. 3), Zhang et al. (2025) found evidence of outflowing molecular gas misaligned with respect to the ionized counterpart (see also García-Burillo et al. 2019). In the following sections, we will discuss in depth the intricate ionized gas properties of the circumnuclear region of NGC 1068, focusing on the low- and high-ionization gas phases, while the investigation of the physical and kinematical properties of the warm molecular counterpart in the entire MIRACLE sample will be addressed in a dedicated forthcoming work.

3.2. Probing the excitation source with Mid-IR and optical diagnostics

To explore the ionization source in the circumnuclear region we took advantage of the wide spectral range covered by our optical and Mid-IR data. In particular, we computed both spatially resolved innovative Mid-IR and standard optical diagnostic diagrams. Among its various science goals, MIRACLE aims at complementing optical tracers of the ionization source with Mid-IR diagnostics, as presented in the following and already showcased in Ceci et al. (2025). In particular, Feltre et al. (2023) showed that transitions occurring in the Mid-IR regime can be pivotal in determining the ionization source in AGN, especially because at such long wavelengths the line flux is poorly affected by dust-attenuation, in contrast to optical transitions. Therefore, following Feltre et al. (2023), we computed the [O IV]/[Ne III] and [Ne III]/[Ne II] line ratios. We note that such transitions fall in different Channels of the MIRI MRS, and therefore the derived maps are characterized by different FoV, spatial PSF and spectral binning. To account for this, we first convolved all the images to the FWHM of the PSF of the reddest transition of the ratio using the *WebbPSF* tool v.1.4.0 (Perrin et al. 2014) and then re-binned all the maps to the coarser pixel size. Finally, to correct for flux discontinuities, which affect both single-pixel and integrated MIRI spectra, we multiplied the flux maps of each channel by the corresponding multiplicative correction factor, derived following the routine presented in Ceci et al. (2025).

Figure 4 shows the Mid-IR and optical ionization diagnostics in the circumnuclear region of NGC 1068, exploiting the [O IV]/[Ne II] vs [Ne III]/[Ne II] (left panels), the [Ne V]/[Ne II] vs [Ne III]/[Ne II] (middle panels), and the [O III]λ5007/Hβ vs [N II]/Hα line ratios (right panels), respectively. In particular, we used model predictions for AGN, SF, and high-velocity shock ionization from Feltre et al. (2023), Gutkin et al. (2016), and

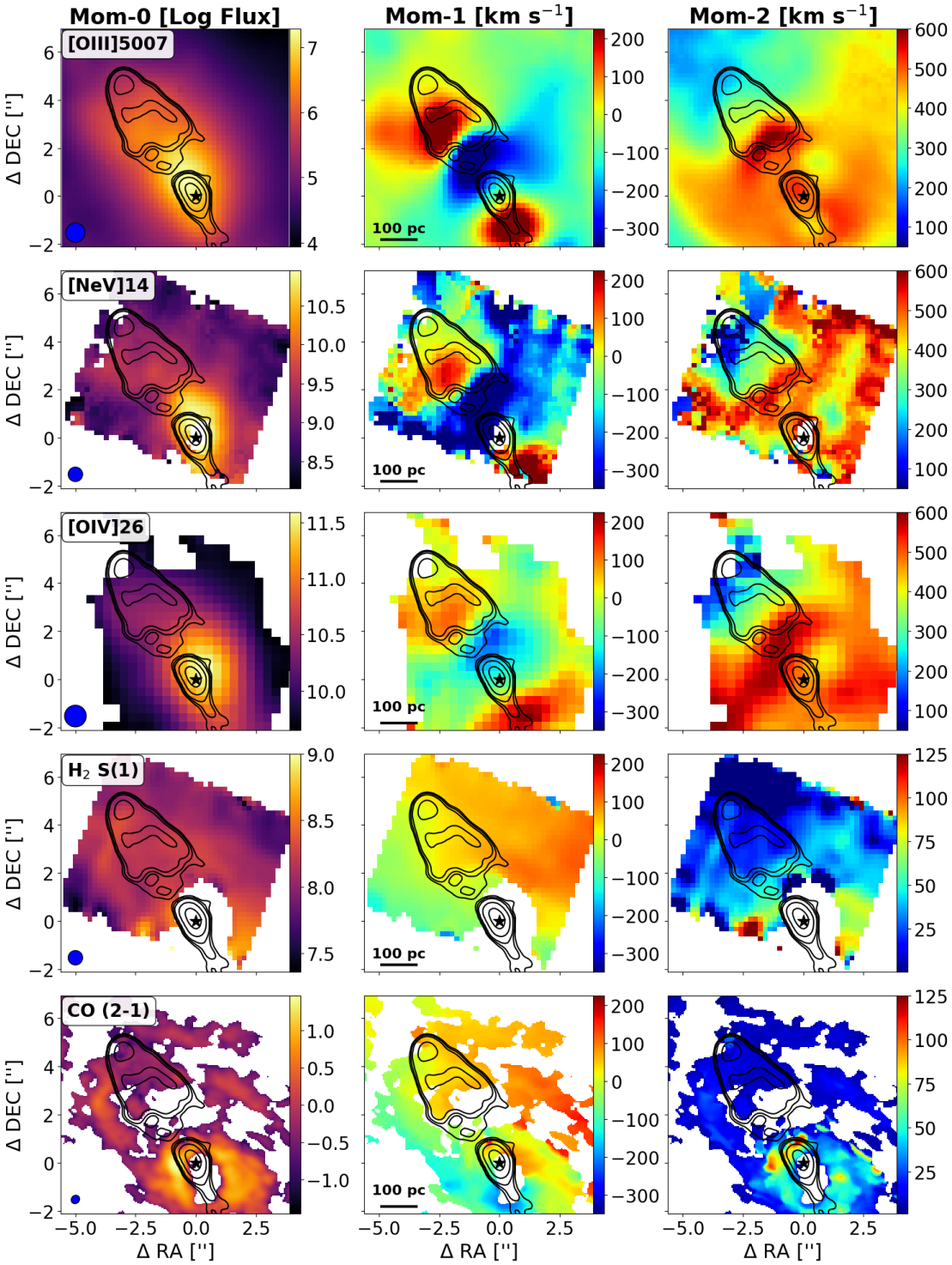

Fig. 3. Moment maps of the various gas phases in NGC 1068. From left to right: integrated line profile (moment 0), LOS velocity (moment 1) and velocity dispersion map (moment 2). From top to bottom: emission from the total line profile of the [O III], [Ne V], [O IV], $H_2S(1)$, and CO (2-1) transitions. The flux maps are in unit of 10^{-20} erg/s/cm^{-2} for MIRI and MUSE, and Jy/beam for ALMA. Black contours represent the same VLA contours of Fig. 1. The black star marks the X-ray inferred nucleus position (Marin et al. 2024). Blue ellipses represent the various instruments beams at the corresponding wavelength of each transition. Spaxels at S/N ≤ 3 are masked.

Alarie & Morisset (2019), respectively, together with demarcation lines from Kewley et al. (2001) and Schawinski et al. (2007) in the optical regime, to estimate the most likely ionization source. Interestingly, the [Ne V]/[Ne II] vs [Ne III]/[Ne II] resolved diagnostic map in Fig. 4 shows a northwest-southeast extended lane compatible with both shock and AGN-driven excitation with an enhanced hourglass-shaped morphology. The remaining spaxels of both Mid-IR diagnostics are instead consistent with pure AGN ionization (for a spatially unresolved analysis see Riffel et al. 2025). The optical diagnostic map suggests that low-ionization (LINER) dominates at the edges of the outflow and the radio-jet morphology, possibly due to the wind im-

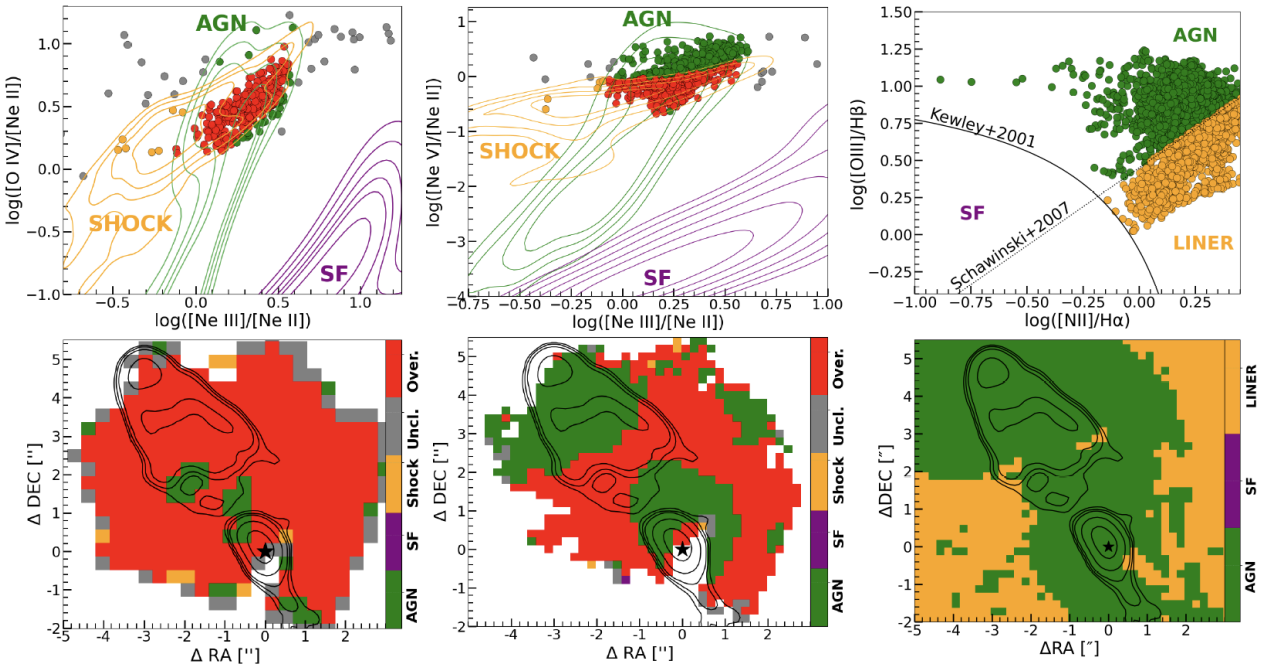

Fig. 4. Ionization diagnostic diagrams for the circumnuclear region of NGC 1068. From left to right: diagnostic exploiting the [Ne III]/[Ne II] vs [O IV]/[Ne II], [Ne III]/[Ne II] vs [Ne V]/[Ne II], and [O III]/Hβ vs [N II]/Hα emission line ratios. Top and bottom panels show the position of each spaxel in the diagnostic diagram and the spatially resolved classification map, respectively. Mid-IR diagnostic models in the first two columns are derived from Feltre et al. (2023). The optical diagnostic shows in solid and dotted black curves the pure star forming region from Kewley et al. (2001) and the demarcation between AGN and LINER ionization from Schawinski et al. (2007), respectively. LINERs-, AGN-, SF-excited spaxels are in orange, green, and purple, respectively. Spaxels in the Mid-IR diagnostics that are not reproducible with any single model and overlapping spaxels are in gray and red, respectively. The black star marks the position of the nucleus. Spaxels with SNR ≤ 3 are masked.

pacting the ISM and shock-heating the gas and to the lower ionization parameter outside the AGN ionization cone, where the AGN excitation dominates. Overall, both the optical and Mid-IR diagnostics reveal that in the circumnuclear region of NGC 1068 no spaxel shows evidence of SF excitation, further corroborating our photoionization model results in Sect. 3.4.3.

3.3. Gas electron density from Mid-IR and optical line ratios

We map the electron density (N_e) in the circumnuclear region exploiting Mid-IR and optical tracers. In particular, for both spectral regimes we employed the PyNeb v1.1.4 package (Luridiana et al. 2015), assuming an isothermal plasma with an electron temperature (T_e) of 10^4 K (Osterbrock & Ferland 2006). We computed spatially resolved maps of the electron density from the flux ratios of the density-sensitive emission lines [Ne V]λ24μm/[Ne V]λ14μm and [Ar V]λ13μm/[Ar V]λ7μm and from the [S II]$\lambda\lambda$6716,6731 doublet. Figure 5 shows the estimated electron density maps obtained with the mentioned line ratios. On average, we found densities of $10^{3.4\pm0.4}$ cm^{-3} and $10^{4.2\pm0.7}$ cm^{-3}, from the neon and argon line ratios. Interestingly, we observe that the neon traces lower densities regions, mostly centered on the nucleus and along the extended outflow, while the argon lines are only detected in a compact knot located $\sim 3''$ (200 pc) northeast of the nucleus and trace higher electron densities. The spatial offset of the argon-traced high-density clump suggests that the highest-density phase of the gas arises in shocked regions, rather than immediately adjacent to the central engine, and likely coincident with the region where the wind and jet impact the galactic disc, and the bow-shock occurs.

As a comparison, the right panel in Fig. 5 shows the optically-derived electron density using the [S II]$\lambda\lambda$6716,6731 doublet. On average, using the optical tracer we find an electron density of $10^{3.6\pm0.4}$ cm^{-3}, which is consistent with the value derived from Mid-IR tracers. Interestingly, comparing the [S II]$\lambda\lambda$6716,6731 and the neon-derived electron density maps we noticed that both show enhanced values of gas density northeast of the nucleus, along the outflow path. Similarly, both maps show lower density lanes around the edges of the [O IV] emission, which is tracing the AGN-driven outflow. Overall, our estimates of the gas electron density from direct estimates using optical and Mid-IR line ratios are consistent with a recent analysis exploiting transauroral line ratios, which reports on average electron densities of $10^{4.4\pm0.4}$ cm^{-3} (Holden & Tadhunter 2023) (see also Sect. 3.4.3). Our estimates of the electron density are also consistent with the findings of Dors et al. (2015) of $10^{4.4}$ cm^{-3} obtained exploiting theoretical calibrations of strong line ratios. Additionally, Revalski et al. (2021) carried out a detailed multi-ionization components CLOUDY modeling, and discussed how the [S II]$\lambda\lambda$6716,6731 emission lines can only probe the low-ionization component, thus yielding a lower density compared to the majority of the gas producing the observed luminosity. Indeed, from the [S II]$\lambda\lambda$6716,6731 line ratio Revalski et al. (2022) found an average density of $10^{3\pm0.3}$ cm^{-3}, consistently with our findings from optical tracers (see also Venturi et al. 2021). On the other hand, exploiting the [S II]$\lambda\lambda$6716,6731 line ratio, Kakkad et al. (2018) found average electron densities within the central 400 pc of $10^{2.8\pm0.2}$ cm^{-3}, which is lower by a factor of $\sim$6 with respect to our estimates, likely due to the fact that they only take into account the flux within the broad components of the [S II]$\lambda\lambda$6716,6731 doublet.

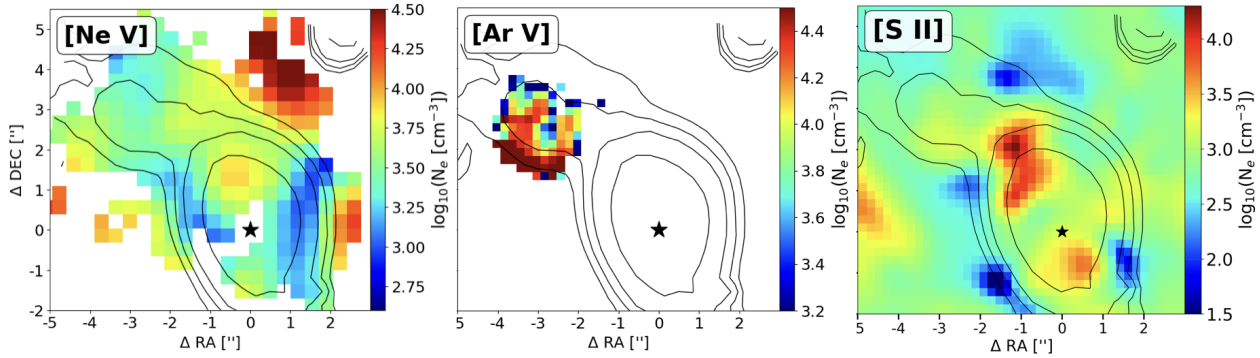

Fig. 5. Resolved maps of the electron density in NGC 1068. The maps are derived from the [Ne V]λ24μm/[Ne V]λ14μm (left), [Ar V]λ13μm/[Ar V]λ7μm (middle), and from the optical [S II]λ6717/[S II]λ6731 (right) line ratios. Black contours are arbitrary flux levels of the [O IV] emission and the black star marks the AGN position.

Table 1. Best-fit parameters for the ionized outflow properties in NGC 1068, traced by [O IV] and [O III] emission lines, as inferred with MOKA^{3D}.

Parameter	Free	[O IV] 26μm	[O III]λ5007
Inclination	Y	76 ± 6	78 ± 3
v_{out} (km s^{-1})	Y	2360 ± 9	2050 ± 12
v_{disp}(km s^{-1})	Y	110 ± 15	125 ± 20
P.A. ($^\circ$)	N	320	320
R_{max}	N	5″ (345 pc)	10″ (690 pc)

From left to right: Parameter, flag indicating whether the parameter is free (Y) or fixed (N), and tracer of a specific gas phases fitted with MOKA^{3D}. The optimized parameters are the outflow inclination, the outflow radial velocity (V_{out}), and the global conical outflow intrinsic velocity dispersion (v_{disp}). The outflow inclination values correspond to the inclination of the cone axis with respect to the LOS. The outflow position angle is kept fixed during the fit. R_{max} is the maximum outflow radius in parsec, set by the limited FoV of the MIRI data. For details on the conical outflow structure and parameters see Sec.3.4.1 .

3.4. Modeling of the ionized outflow

To investigate the gas kinematic and ionization conditions in the circumnuclear region of NGC 1068, leveraging both MIRI and MUSE data, we exploited our innovative multi-cloud kinematic (MOKA^{3D}; Marconcini et al. 2023, 2025b) and photo-ionization (HOMERUN; Marconi et al. 2024) models.

3.4.1. Tracing the outflow kinematics with MOKA^{3D}

MOKA^{3D} is a 3D multi-cloud kinematic model designed to account for the clumpy structures observed in spatially resolved data. As a result, it provides the intrinsic 3D de-projected gas kinematics. Crucially, rather than prescribing an analytic surface-brightness profile, MOKA^{3D} assigns a weight to each model cloud proportional to the line flux observed in each volumetric pixel, thereby reproducing the observed clumpy morphology and complex line profiles. In the following analysis the free parameters are the outflow radial velocity (v_{out}) and the cone inclination with respect to the LOS, which are varied to minimize the residuals between model and observed spectra in each spaxel. To account for the complex ionized gas kinematics observed in our data, the best MOKA^{3D} model is a bi-conical outflow, with a position angle (P.A.) of 320°[2], inner and outer semi-opening angle of 0°-55°, and a maximum radius of 5″ (345 pc) and 10″ (690 pc) to model the Mid-IR and optical [O IV] and [O III] emission, respectively. Exploiting the high angular resolution of MIRI and MUSE data, we were able to infer the outflow radial velocity and inclination profiles as a function of the distance from the nucleus for the warm and highly ionized phases. To investigate the outflow radial velocity profile traced by the [O IV] ([O III]) emission in MIRI (MUSE), we divided the conical model into five (eleven) concentric conical shells of width 1″ (0.9″) and assumed that the outflow velocity and the inclination in each shell remain constant. The number of shells is set by the data spatial resolution and the maximum extent of the model. Indeed, we first set the maximum extent of the model and then set the width of each shell to be equal to the full width at half maximum (FWHM) of the point spread function (PSF), in order to take full advantage of the data spatial resolution. Figure C.1 in Appendix C shows the comparison between the observed and best-fit moment maps for the [O III] and [O IV] emission, obtained with the best-fit parameters inferred by the multi-shell MOKA^{3D} fit. Additionally, we also performed a fit with a single radial velocity and no shells to infer the single best-fit velocity and inclination that reproduce the observed features. Our spatially-averaged findings are consistent with previous kinematic analysis (see Tab. 1 and e.g. Das et al. 2006; Barbosa et al. 2014). Interestingly, we notice that, despite having the same aperture and consistent inclinations, the [O IV] traces an outflow that is faster by ~ 300 km s^{-1} compared to the lower ionization [O III] counterpart, hinting at two separate kinematic components within the same geometry or, alternatively, at the key role in the attenuation which might be dampening the optical outflowing emission. Figure 6 shows a schematic representation of the multiple kinematic components in NGC 1068. In particular, the northeast and southwest cones lie above and below the galaxy disc, respectively, and are coaxial to the radio jet, as supported by multi-wavelength and multi-scale analysis (Barbosa et al. 2014; Venturi et al. 2021; Mutie et al. 2024). The approaching (receding) cone is propagating along the blueshifted (redshifted) side of the galactic disc, as shown by the underlying stellar kinematics in Fig. 6. The blue and red clouds along each side of the ionization cone represent gas displaced along the approaching and receding side of the cone, respectively, and are modeled by giving different weights to the blue and red clouds in the cone (see top three panels in Fig. 3 and Fig. C.2).

[2] Measured clock-wise from the North. See Marconcini et al. (2023) for a detailed description of the model parameters.

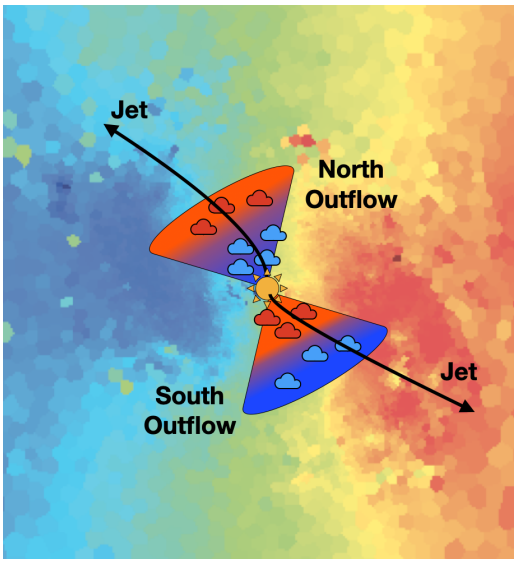

Fig. 6. Schematic representation of the main kinematic components in the circumnuclear region of NGC 1068. The underlying map shows the stellar kinematic derived from optical MUSE data with the routine described in Appendix B. The bi-conical outflow is colored based on the observed and modeled LOS ionized gas velocity, with blue (red) clouds approaching (receding) the observer. The yellow sun and black arrows illustrate the AGN position and the radio-jet, respectively.

Figure 7 displays the radial profile of the outflow velocity as inferred for the [O IV] and [O III] emission lines in NGC 1068, compared to previous ionized outflow velocity profiles inferred with the same methodology by Marconcini et al. (2025b) in a sample of local AGN. Interestingly, as shown in Fig. 7, MUSE data reveal that the outflow in NGC 1068 is characterized by a peak velocity at $\sim$ 160 pc from the nucleus, followed by a smooth deceleration up to $\sim$ 500 pc. Then, the outflow velocity increases up to its maximum extent, consistently with the trend found by Marconcini et al. (2025b). The [O IV] profile shows a similar trend, with an almost constant radial velocity up to $\sim$ 200 pc, followed by a smooth deceleration up to the maximum scale traced by MIRI observations of $\sim$ 345 pc. Unfortunately, due to the limited FoV of our MIRI data, we cannot conclusively state whether the highly-ionized phase traced by [O IV] is accelerating on larger scales similarly to the warm ionized counterpart traced by [O III]. Zubovas & Tartėnas (2025) carried out analytic calculations and demonstrated that the observed velocity trend of the sample presented in Marconcini et al. (2025b) can be reproduced assuming a pure energy-driven outflow expanding in a bulge with an isothermal density distribution and finite extent. We will address such a scenario in the following section.

3.4.2. Energy-driven model for AGN-driven outflows

One of the most promising theoretical frameworks explaining the propagation of galactic outflows is the AGN wind-driven outflow model (for a review, see King & Pounds 2015). Within this scenario, the AGN radiation field launches a quasi-relativistic wind from the accretion disc, which carries $\sim$ 5% of the AGN bolometric luminosity as kinetic energy rate. The wind shocks against the surrounding ISM, heats it to a temperature $\sim 10^{10}$ K and causes the expansion of a massive outflow. In most cases, the shocked wind bubble is approximately adiabatic (Faucher-Giguère & Quataert 2012), so the outflow is driven by the whole wind energy input. This leads to a relatively fast outflow, with $v_{\rm out} \gg \sigma_{\rm bulge}$. If the gas density profile is isothermal, i.e. $\rho \propto R^{-2}$, the outflow quickly reaches a constant velocity. In general, a shallower density profile leads to deceleration, while a steeper profile leads to an accelerating outflow. If the gas distribution has a limited spatial extent, as expected for a galactic bulge, the outflow should accelerate after escaping the bulge. Note that low power jets in AGN – as in NGC 1068 – are found to have little to no contribution in regulating either the morphology or mass of outflows and are therefore neglected in the following analysis (e.g., Mukherjee et al. 2016; Tanner & Weaver 2022).

To investigate the propagation of an energy-driven outflow in a multi-component bulge and halo system, we used the 1D outflow evolution calculator MAGNOFIT (Zubovas et al. 2022), which solves the equation of motion of an adiabatic outflow in a generic gravitational potential and gas density distribution. We found that the superposition of a multi-component bulge and halo system (inner cavity, bulge, rarefied halo) is able to reproduce the observed outflow velocity profile (see the top panel in Fig. 7). The inner two regions of the model comprise the galaxy bulge with a total mass of $2.9 \times 10^9 M_\odot$ and a gas fraction of $f_{\rm g} = 6.8 \times 10^{-3}$, consistently with the findings of Das et al. (2006). On the other hand, Meena et al. (2023) found a total bulge mass almost one order of magnitude larger than our analysis, probably due to the larger effective bulge radius they assumed and to their purely photometric analysis. To further motivate the choice of an inner cavity within the bulge, at the bottom panel of Fig. 7 we show the best-fit density profile obtained with MAGNOFIT and the light-profile of the $H_2S(1)$, as a proxy of the molecular gas mass. Figure 7 clearly shows a depletion of molecular gas within the central $\sim$140 pc, as confirmed by moment maps in Fig. 3 (see also García-Burillo et al. 2014) and a rise lasting up to $\sim$ 400 pc which is co-spatial with the bow-shock (see App. F; Mutie et al. 2024), likely suggesting an enhancement of the warm molecular transitions in the warm shocked medium (Kristensen et al. 2023). Beyond R$\sim$0.4 kpc, the bulge ends and only a halo following the prescription of Navarro et al. (1997) with $f_{\rm g} = 10^{-3}$ remains. As suggested in Zubovas & Tartėnas (2025), the low density allows the outflow to accelerate significantly up to $\sim$ 4 kpc, although later it slows down due to the relatively flat halo density profile in the central $\sim$ 20 kpc. In Sect. 3.6 we will discuss the implications of these results in the broader context of AGN feedback and evaluate the energetic impact of the wind onto its host.

3.4.3. Estimating gas physical properties with HOMERUN

The HOMERUN model uses a weighted superposition of grids of "single-cloud" CLOUDY models (Ferland et al. 1998), each defined by a specific ionization parameter (U), hydrogen density ($n_{\rm H}$), metallicity (Z) and ionizing spectrum (see App. D for details). The advantage of HOMERUN with respect to standard methods to estimate the gas physical properties (see e.g. Méndez-Delgado et al. 2023), is that it assign weights to these artificial clouds, which are treated as free parameters and are optimized via a non-negative least squares fit to all observed emission-line fluxes. By fitting all different model grids in gas-phase metallicity and ionizing continuum, HOMERUN identifies the grid with the best combination of single-cloud models that reproduces the observed line fluxes, thus providing robust estimates of the gas properties including metallicity, ionization parameter, attenuation, and density.

We infer the ionized gas properties across the wavelength range covered by MIRI and MUSE considering the largest FoV

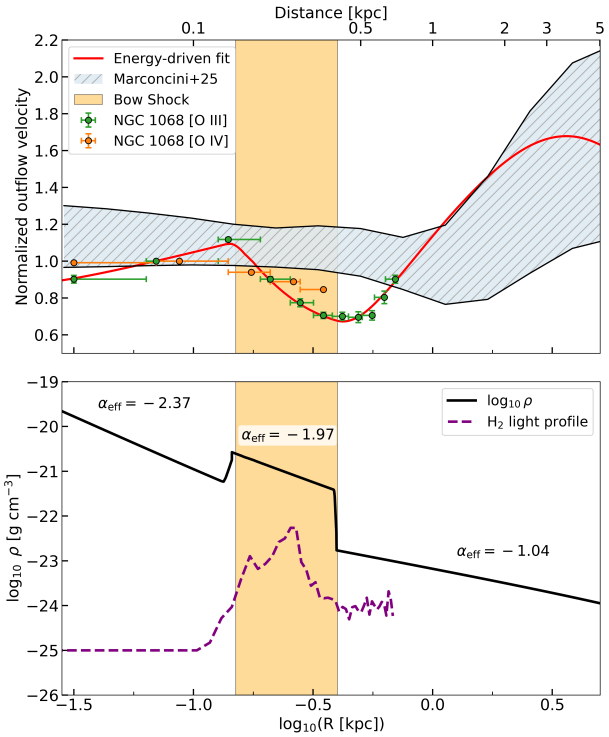

Fig. 7. Outflow radial velocity and best-fit energy driven profiles. Top panel: Green and orange points represent the best fit of the outflow radial velocity in each shell for NGC 1068 traced by [O III], [O IV], respectively. Solid red line represents the best-fit of the outflow velocity profile in NGC 1068 with MAGNOFIT (see Sect. 3.4.2). The outflow velocity profiles are normalized to the mean outflow velocity within the distance at which the minimum outflow velocity for each target occurs. The shaded gray region represents the radial velocity profile of the sample analyzed in Marconcini et al. (2025b) considering the 16-84 percentiles at any radius. Bottom panel: The black solid line represents the gas density profile of the best-fit MAGNOFIT model. Density slopes of each segment of the best-fit density profile are shown. The dashed purple curve represents the scaled H_2S(1) light profile as a proxy of the molecular mass distribution. The shaded yellow region represents the distance covered by the bow shock (see App. F and Mutie et al. 2024).

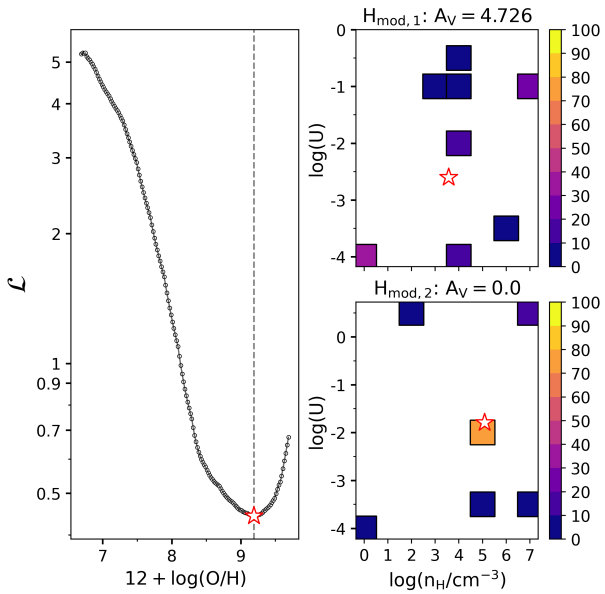

Fig. 8. HOMERUN results for NGC 1068. Left panel: variation of the loss function $\mathscr{L}$ as a function of the oxygen abundance. The deep minimum (white star) of the $\mathscr{L}$ curve represents the best-fit metallicity at $\mathscr{L}$ = 0.44. Right panels: grids of single-cloud models in log(U) and log(N_H) for the AGN and SF components. The colors represent the weights of each single-cloud best-fit model. The white star represents the weighted density and ionization parameter of the single-cloud models for each AGN component.

available in both observations, i.e. the MIRI Ch1 FoV ($3.2'' \times 3.7''$). We extracted the integrated Mid-IR and optical spectrum from such an aperture and computed the line fluxes and uncertainties, for a total of 26 Mid-IR and 28 optical transitions. In such aperture the AGN is the main ionization source for the ionized gas (see Fig. 4), as also suggested by the presence of highly-ionized transitions (e.g. [Mg V], [Ne V], [Ne VI]). Moreover, our kinematic analysis suggests that all ionized gas tracers are likely entrained into the AGN-driven outflow due to the observed high-velocities and the absence of either ordered disc-like motions (see Fig. 3) and SF excitation (see Fig. 4). For such reasons, we consider the AGN radiation field as the only source of ionizing photons in our models that is able to account for the emission of gas ionized by the AGN. In App. D we also show the best-fit results obtained by adopting a combination of AGN and star formation (SF) models, which is not able to properly reproduce the observed ionized gas emission line fluxes. To fit the observed optical + Mid-IR set of emission lines we opted for a combination of two grids of AGN models (Homerun Model 1 and Model 2, hereafter $H_{mod,1}$ and $H_{mod,2}$). The two components are represented by two grids of AGN models, with ($H_{mod,1}$) and without ($H_{mod,2}$) dust, with the same AGN continuum and metallicity but subject to different attenuation. The choice of including dust-free models is motivated by the detection of optical and Mid-IR iron transitions (see Fig. 2), which are predominantly depleted on dust-grains. Nevertheless, we found that dust-free AGN models only are not able to reproduce the entire set of optical+Mid-IR emission lines, motivating the need for dust-rich models. Given the complexity of the line profiles and the blending among the lines (e.g. Hα + [N II] complex), we decide to use 20% as our "acceptable" discrepancy between model and observations. The observed Mid-IR ionized emission line fluxes are mostly reproduced by the dust-rich $H_{mod,1}$ component, with average extinction of $A_V = 4.726$, density of $\log(n_H / cm^{-3}) = 3.5$, and ionization parameter of $\log(U) = -2.7$. On the other hand, the $H_{mod,2}$ component is characterized by no dust attenuation, $\log(n_H / cm^{-3}) = 5.1$, and $\log(U) = -1.8$ (for details see App. D and Fig. 8) and is found to dominate the optical transitions. In the following we assume $n_H = N_e$ as the gas can be regarded as fully ionized over the regions considered in this analysis. Under this assumption, we notice that the HOMERUN estimates of the gas electron density are consistent with the direct method estimates presented in Sect. 3.3.

Figure 8 shows the loss function $\mathscr{L}$ which is minimized to retrieve the best-fit parameters of interest (for details see Marconi et al. 2024) and determines a gas-phase metallicity of 9.19 (i.e. $Z \sim 3\ Z_\odot$). Our estimate of the metallicity in NGC 1068 is consistent with previous photoionization model estimates (Castro et al. 2017) and is slightly larger with respect to estimates based on strong line calibrations (Dors & Copetti 2006; Armah et al. 2024), likely because such calibrations assume simplified physical conditions (e.g., uniform temperature and ionization) neglecting any structure of the NLR. The main advantage of using HOMERUN to infer the ionized gas properties is that it allows for a direct rescaling of the total line luminosity to the gas mass without the need to correct the flux for the attenu-

ation, which is instead directly estimated by the model. The luminosity-to-mass conversion can be simply expressed as:

$$M_{\rm ion} = C_{\rm line} \times L_{\rm line}, \quad (1)$$

where $L_{\rm line}$ is the observed line luminosity not corrected for attenuation and $C_{\rm line}$ is the coefficient derived from the HOMERUN $H_{\rm mod,1}$ ($C_{\rm line,1} = 2.8 \times 10^5$ $M_\odot/[10^{40}$ erg/s]) and $H_{\rm mod,2}$ ($C_{\rm line,2} = 1.3 \times 10^2$ $M_\odot/[10^{40}$ erg/s]) AGN models. Such a factor allows us to convert the observed emission line luminosity to ionized mass taking into account the dust attenuation. For the [O IV] transition, the best-fit yield $C_{\rm line,1} = 2.6 \times 10^5$ $M_\odot/[10^{40}$ erg/s] and $C_{\rm line,2} = 1.2 \times 10^2$ $M_\odot/[10^{40}$ erg/s] for the $H_{\rm mod,1}$ and $H_{\rm mod,2}$ model, respectively. We stress that HOMERUN finds that the [O III] and [O IV] transitions are dominated by the dust-poor and dust-rich AGN grids, respectively. Such a result independently supports the different outflow velocity between the [O III] and [O IV] transitions, as inferred in Sect. 3.4.1. Finally, such a robust method allows us to directly estimate the ionized gas mass at unprecedented accuracy of $M_{\rm out}$([O III]) = (5.920 $\pm$ 0.006)$\times$ 10^6 $M_\odot$ and $M_{\rm out}$([O IV]) = (7.1$\pm$ 1.2) $\times$ 10^6 $M_\odot$ (see also Tab. 2).

3.5. Unveiling the outflow impact on its host

In this section we estimate the ionized outflow energetics, i.e. its mass outflow rate ($\dot{M}_{\rm out} = M_{\rm out} v_{\rm out}/\Delta R$), kinetic energy ($E_{\rm out} = \frac{1}{2} M_{\rm out} v_{\rm out}^2$), momentum rate ($\dot{p} = \dot{M}_{\rm out} v_{\rm out}$), and kinetic power ($\dot{E}_{\rm out} = \frac{1}{2} \dot{M}_{\rm out} v_{\rm out}^2$), exploiting the mass estimate from HOMERUN and the kinematics from MOKA^{3D} and we compare them to the values obtained with the standard approach (for details see App. H and Cano-Díaz et al. 2012; Carniani et al. 2015; Cresci et al. 2015). Combining the estimates of the outflow properties inferred with these models carries many advantages with respect to standard methods. These include taking into account projection effects, the spatial PSF of the data and directly inferring the gas ionization, temperature and metallicity (for more details see Marconcini et al. 2023; Marconi et al. 2024). Ceci et al. (2025) carried out the first detailed comparison of the outflow energetics computed with standard assumptions and with innovative multi-cloud models HOMERUN + MOKA^{3D} showcasing the large limitations of the standard approach, which lead to severely underestimated masses and consequently unreliable mass outflow rates, especially for highly ionized transitions.

Table 2 shows the comparison of the outflow energetics estimates obtained by adopting the standard approach and the innovative MOKA^{3D}+ HOMERUN technique. Adopting a bolometric luminosity of log($L_{\rm bol}$/erg s^{-1}) = 45.1$\pm$0.5 (GRAVITY Collaboration et al. 2020) we normalized the kinetic energy and momentum rate to $L_{\rm bol}$ to quantitatively assess the impact of the ionized outflow on the host in terms of star formation quenching and energy injected in the ISM per unit of time. Overall, the energetic properties derived with the standard method are in agreement with the estimates of the outflow energetics from previous analysis, as expected since they rely on the same assumptions (Müller-Sánchez et al. 2011; Barbosa et al. 2014; Revalski et al. 2021, 2022; Holden & Tadhunter 2023). On the other hand, the results inferred with MOKA^{3D}+ HOMERUN are systematically larger of up to two orders of magnitude compared to the standard method findings. Such a discrepancy has to be mainly ascribed to the advantages carried by the Mid-IR regime in inferring the intrinsic ionized gas mass content and to the difference in the line luminosity to mass conversion factor ($C_{\rm line}$) in Eq. 1, which with our methodology is $\sim 10^2$ times larger compared to the standard method value outlined in App. H. We stress that the luminosity-to-mass conversion factor from the dust-free AGN model $H_{\rm mod,2}$ is comparable to the value estimated in App. H, e.g. 130 vs 147 for the [O III]. Our findings showcase the importance of combining innovative tools – such as HOMERUN and MOKA^{3D}– with a multi-wavelength analysis. Indeed, such a strategy allowed us to unveil a massive, hidden ionized gas component which completely revolutionizes the impact of the ionized outflow on its host.

The large coupling efficiency ($\varepsilon_{\rm kin} = \dot{E}_{\rm out}/L_{\rm bol}$) and momentum boost ($\dot{p}/(L_{\rm bol}/c)$) listed in Table 2 indicate efficient conversion of the AGN radiative energy into the outflow kinetic energy, suggesting that the outflow is able to highly perturb and unbind the gas (Zubovas & King 2012; Costa et al. 2014), possibly driving the observed enhanced velocity dispersion lane perpendicular to the outflow and jet direction (see Fig. 3 and Wagner et al. 2012; Mukherjee et al. 2018a; Venturi et al. 2021). A large coupling efficiency directly translates into heating and removal of a large amount of gas from the host as well as star formation quenching in the circumnuclear region, consistently with the role played by energy-conserving winds and in agreement with our findings in Sect. 3.4.2 (see also Farcy et al. 2025).

To independently quantify the role of the outflow in expelling the material out of the host gravitational potential we compare the outflow velocity to the escape velocity. Following the prescription of Veilleux et al. (2020), we can conservatively assume the escape velocity at the outflow maximum extent as $v_{\rm esc} = 3 \times v_{\rm circ}$, with $v_{\rm circ}$ the circular velocity of the disc at the maximum distance reached by the wind. In App. G we performed a kinematic fit of the disc component traced by the ionized gas up to a de-projected scale of 50″ ($\sim$ 3.4 kpc) from the nucleus. In particular, we find that the $v_{\rm circ}$(345 pc) = 90$\pm$ 25 km s^{-1} and $v_{\rm circ}$(690 pc) = 120$\pm$ 25 km s^{-1}, which yield an escape velocity of 270$\pm$ 75 and 360 $\pm$ 75 km s^{-1}, respectively. Finally, we estimate $v_{\rm out}/v_{\rm esc}$ = 7.3 (3.7) at 345 (900)pc. Therefore, we found $v_{\rm out}/v_{\rm esc} \gg 1$ at any radius, confirming that the outflowing gas is unbound to its host and thus will not fall back onto the nucleus, with the potential to not only reduce the amount of gas that can accrete onto the central SMBH but to also sweep away the fuel for star formation.

Our estimates of the outflow momentum boost traced by the ionized gas phase are consistent with values derived in surveys of molecular outflows in the local Universe (Cicone et al. 2014; Fluetsch et al. 2019), yet larger compared to what is expected for local ionized outflows (Harrison et al. 2014; Fiore et al. 2017). Overall, both the large coupling efficiency and momentum boost confirm the scenario of an energy-conserving expanding outflow and possibly suggest a non negligible contribution from the co-spatial radio-jet in driving the ionized outflow due to jet mechanical work, which likely raises the effective observed energy and momentum beyond what expected from the purely radiative $L_{\rm bol}$ input only (Zubovas & King 2012; Faucher-Giguère & Quataert 2012; Costa et al. 2014; García-Burillo et al. 2014; Mukherjee et al. 2018a; Longinotti et al. 2023; Farcy et al. 2025).

3.6. Outflow stratification or dust-enshrouded high velocity clouds?

The warm and highly ionized outflow components share a similar velocity profile with a difference of $\sim$ 300 km s^{-1} (Sect. 3.4.1), while the observed velocity profile is well fitted by an energy-driven wind transitioning from a bulge with finite extent into a rarefied halo (Sect. 3.4.2), consistent with recent trends (Zubovas & Tartėnas 2025).

Table 2. Ionized outflow energetic properties in NGC 1068 traced by [O IV] and [O III] emission lines.

	[O IV] 26μm		[O III]λ5007	
	HR	Std	HR	Std
M_{out} (10^4 $M_\odot$)	709^{+119}_{-119}	$3.3^{+1.0}_{-0.7}$	$592.0^{+0.6}_{-0.6}$	11^{+5}_{-3}
$\dot{M}_{out}$ ($M_\odot$/yr)	83^{+15}_{-14}	$0.4^{+0.1}_{-0.1}$	60^{+4}_{-3}	$1.2^{+0.4}_{-0.4}$
E_{out} (10^{54} erg)	392^{+66}_{-65}	$1.8^{+0.5}_{-0.5}$	247^{+3}_{-3}	$4.8^{+1.7}_{-1.7}$
$\dot{E}_{out}$ (10^{41} erg/s)	1457^{+270}_{-255}	$6.8^{+1.9}_{-1.7}$	798^{+56}_{-50}	16^{+6}_{-5}
$\dot{p}$ (10^{33} dyne)	1234^{+228}_{-215}	$5.8^{+1.5}_{-1.5}$	778^{+53}_{-47}	15^{+6}_{-5}
$\dot{p}/(L_{bol}/c)$	15^{+13}_{-5}	$0.07^{+0.06}_{-0.03}$	9^{+8}_{-3}	$0.2^{+0.2}_{-0.1}$
ε_{kin} (%)	6^{+5}_{-2}	$0.03^{+0.02}_{-0.01}$	3^{+2}_{-1}	$0.06^{+0.6}_{-0.3}$

Notes. From top to bottom: outflow mass (M_{out}), mass outflow rate ($\dot{M}_{out}$), kinetic energy (E_{out}), kinetic power ($\dot{E}_{out}$), momentum rate ($\dot{p}$), momentum boost ($\dot{p}/(L_{bol}/c)$), and coupling efficiency (ε_{kin}). The values are derived from the integrated analysis over the 1.5″ radius aperture using the MOKA^{3D} tool to estimate the kinematic and geometry and HOMERUN (HR) to estimate the masses (see Sect. 3.4.1-3.4.3). As a comparison, we list the estimates obtained with the standard approach (Std), following the procedure outlined in App. H. The uncertainties on the outflow energetics are estimated via a Markov Chain Monte Carlo analysis with 10^4 iterations adopting the 16-84 percentiles of the posterior distribution as the 1σ confidence interval.

Previous works based on spatially integrated analysis interpreted the correlation between larger line width, which is a proxy of the outflow velocity, and the IP as evidence for outflow deceleration as larger IP transitions are expected to origin closer to the central engine (e.g. Armus et al. 2023). Here we propose an alternative scenario and ascribe previous interpretations to the lack of a spatially resolved analysis and physically-motivated modeling. Indeed, consistently with previous studies, we found that [O IV] (IP = 55 eV) has a larger velocity compared to [O III] (IP = 35 eV), but we demonstrated that [O IV] is not originating closer to the AGN compared [O III] and that the correlation between line width and IP is not indicative of an outflow deceleration as both transition can be co-spatial.

Our HOMERUN results indicate that the observed [O III] and [O IV] emission originate from two different components, respectively dust-poor and dust-rich. As a result, since the [O IV] transition fell in the poorly attenuated Mid-IR spectral regime, it offers the unique possibility to unveil the intrinsic outflow kinematics. On the other hand, due to the large dust content in the dominant $H_{mod,1}$ component ($A_V = 4.726$), the high-velocity outflow component that contributes to the line wings is deeply attenuated in the optical regime and is therefore not detected in optical transitions, leading to an underestimation of the [O III]-traced outflow velocity. Our findings suggest that both transitions originate from the same dust-rich regions (see Fig. 3) and that no velocity stratification is present within the outflow. Our results highlight the key role of spatially resolved Mid-IR observations to unveil the dust-enshrouded circumnuclear emission and stress the necessity for comprehensive models to interpret multi-wavelength observations.

4. Conclusions

In this work we presented a multi-phase overview of the gas properties in NGC 1068, exploiting new MIRI/MRS data from the MIRACLE program. We complemented our analysis with MUSE, ALMA, and VLA observations. We mainly focused on the ionized outflow as traced via multiple emission lines and evaluated its impact on the host comparing its properties with the galaxy and radio jet morphologies. The main conclusions from this work are the following:

- We detected more than 20 emission lines tracing the ionized gas with an IP from a few eV up to $\sim$ 180 eV and seven warm molecular pure-rotational transitions (see Fig. 2 and Table D.1).
- Moment maps of the ionized and molecular phases shown in Fig. 3 highlight their different morphologies and kinematics, with the molecular and ionized gas tracing the galaxy disc and the bi-conical outflow, respectively.
- We modeled the ionized outflow with the kinematic tool MOKA^{3D} exploiting both the [O IV] and [O III] emission lines. We found velocities $\geq$ 2000 km s^{-1} and a systematic difference of 300 km s^{-1} between the warm ([O III]) and highly ionized ([O IV]) phases. The large FoV of MUSE allows to trace the outflow properties up to $\sim$ 700 pc from the center, showing evidence of gas acceleration starting at $\sim$ 500 pc from the nucleus (Fig. 7) consistent with recent theoretical model predictions.
- Mid-IR and optical emission-line ratios highlight a major AGN ionization across the circumnuclear region of NGC 1068 and in particular along the outflow direction (Fig. 4) with hints of LINER ionization at the outflow edges.
- Independent Mid-IR and optical emission line ratios were used to compute spatially resolved electron density maps (see Fig. 5), which revealed clumpy structures of various density along the ionized outflow ($n_e \sim 10^{2-5}$ cm^{-3}).
- The outflow properties were compared to state-of-the-art theoretical predictions to confirm the pure energy-driven scenario for the outflow. We exploited the innovative photoionization tool HOMERUN and demonstrated that the intrinsic energetic of the ionized outflow in NGC 1068 has been largely underestimated. This finding has profound consequences in terms of the real impact of the outflow on the host galaxy evolution. We quantified the impact of the ionized outflow on its host by showing that a large amount of energy is injected in the ambient ISM, preventing star formation by both sweeping away and heating the ambient gas. The large outflow energetics also suggests a possible contribution from the co-spatial radio-jet in driving the outflowing gas and injecting large mechanical work.

We quantitatively demonstrate the crucial importance for a multi-wavelength approach and the adoption of physically-motivated models to account for the observed complex physical properties of the gas, while highlighting the limitations of standard approaches. Our findings illustrate the drastic change of scenario that can emerge when properly evaluating the true outflow energetics, leading to quantitatively different conclusions on the capability of AGN-driven outflows to regulate the evolution of their host galaxies.

Acknowledgements. All the authors acknowledge the MIRACLE INAF 2024 GO grant "A JWST/MIRI MIRACLE: Mid-IR Activity of Circumnuclear Line Emission". CM, GC, AM, FM, EB, GV and AF acknowledge the support of the INAF Large Grant 2022 "The metal circle: a new sharp view of the baryon cycle up to Cosmic Dawn with the latest generation IFU facilities". CM, GC, AM, FM, EB also acknowledge the support of the grant PRIN-MUR 2020ACSP5K_002 financed by European Union – Next Generation EU. AM, FM, GC, IL acknowledge support from project PRIN-MUR project "PROMETEUS" financed by the European Union - Next Generation EU, Mission 4 Component 1 CUP B53D23004750006. MM is thankful for support from the European Space

Agency (ESA). AF and EB acknowledge financial support from the Ricerca Fondamentale INAF 2024 under project 1.05.24.07.01 MiniGrant RSN1. AVG acknowledges support from the Spanish grant PID2022-138560NB-I00, funded by MCIN/AEI/10.13039/501100011033/FEDER, EU. GS acknowledges financial support under the National Recovery and Resilience Plan (NRRP), Mission 4, Component 2, Investment 1.1, Call for tender No. 104 published on 2.2.2022 by the Italian Ministry of University and Research (MUR), funded by the European Union – NextGenerationEU-Project Title 2022JC2Y93 Chemical Origins: linking the fossil composition of the Solar System with the chemistry of protoplanetary disks – CUP J53D23001600006 – Grant Assignment Decree No. 962 adopted on 30.06.2023 by the Italian Ministry of Ministry of University and Research (MUR); the project ASI-Astrobiologia 2023 MIGLIORA ("Modeling Chemical Complexity", F83C23000800005); the INAF-GO 2024 fundings ICES, the INAF-GO 2023 fundings PROTOSKA ("Exploiting ALMA data to study planet forming disks: preparing the advent of SKA", C13C23000770005) and the INAF Minigrant 2023 TRIESTE ("TRacing the chemIcal hEritage of our originS: from proTostars to planEts"). IEL acknowledges support from the Cassini Fellowship program at INAF-OAS. FS acknowledges support from the PRIN MUR 2022 2022TKPB2P - BIG-z, Ricerca Fondamentale INAF 2023 Data Analysis grant 1.05.23.03.04 "ARCHIE ARchive Cosmic HI & ISM Evolution", Ricerca Fondamentale INAF 2024 under project 1.05.24.07.01 MINI-GRANTS RSN1 "ECHOS", Bando Finanziamento ASI CI-UCO-DSR-2022-43, CUP C93C25004260005, project "IBISCO: feedback and obscuration in local AGN". These observations are associated with program 6138. MT and KZ are funded by the Research Council Lithuania grant no. S-MIP-24-100. The authors acknowledge the team led by coPIs Cosimo Marconcini and Anna Feltre for developing their observing program with a zero-exclusive-access period. This work is based on observations made with the NASA/ESA/CSA JWST. The data were obtained from the Mikulski Archive for Space Telescopes at STScI, which is operated by the Association of Universities for Research in Astronomy, Inc., under NASA contract NAS 5-03127 for JWST. The specific observations analyzed can be accessed via doi: https://doi.org/10.17909/b4w1-hk44.

References

Alarie, A. & Morisset, C. 2019, Rev. Mexicana Astron. Astrofis., 55, 377
Armah, M., Riffel, R., Dahmer-Hahn, L. G., et al. 2024, MNRAS, 534, 2723
Armus, L., Lai, T., U, V., et al. 2023, ApJ, 942, L37
Asplund, M., Amarsi, A. M., & Grevesse, N. 2021, A&A, 653, A141
Asplund, M., Grevesse, N., Sauval, A. J., & Scott, P. 2009, ARA&A, 47, 481
Audibert, A., Ramos Almeida, C., García-Burillo, S., et al. 2023, A&A, 671, L12
Bacon, R., Accardo, M., Adjali, L., et al. 2010, in Society of Photo-Optical Instrumentation Engineers (SPIE) Conference Series, Vol. 7735, Ground-based and Airborne Instrumentation for Astronomy III, ed. I. S. McLean, S. K. Ramsay, & H. Takami, 773508
Barbosa, F. K. B., Storchi-Bergmann, T., McGregor, P., Vale, T. B., & Rogemar Riffel, A. 2014, MNRAS, 445, 2353
Bland-Hawthorn, J., Gallimore, J. F., Tacconi, L. J., et al. 1997, Ap&SS, 248, 9
Bushouse, H., Eisenhamer, J., Dencheva, N., et al. 2022, spacetelescope/jwst: JWST 1.6.2
Cano-Díaz, M., Maiolino, R., Marconi, A., et al. 2012, A&A, 537, L8
Capetti, A., Axon, D. J., & Macchetto, F. D. 1997, ApJ, 487, 560
Cappellari, M. & Copin, Y. 2003, MNRAS, 342, 345
Cappellari, M. & Emsellem, E. 2004, PASP, 116, 138
Carniani, S., Marconi, A., Maiolino, R., et al. 2015, A&A, 580, A102
CASA Team, Bean, B., Bhatnagar, S., et al. 2022, PASP, 134, 114501
Castro, C. S., Dors, O. L., Cardaci, M. V., & Hägele, G. F. 2017, MNRAS, 467, 1507
Ceci, M., Marconcini, C., Marconi, A., et al. 2025, arXiv e-prints, arXiv:2507.08077
Cecil, G., Bland, J., & Tully, R. B. 1990, ApJ, 355, 70
Cicone, C., Brusa, M., Ramos Almeida, C., et al. 2018, Nature Astronomy, 2, 176
Cicone, C., Maiolino, R., Sturm, E., et al. 2014, A&A, 562, A21
Costa, T., Sijacki, D., & Haehnelt, M. G. 2014, MNRAS, 444, 2355
Crenshaw, D. M. & Kraemer, S. B. 2000, ApJ, 532, L101
Cresci, G., Marconi, A., Zibetti, S., et al. 2015, A&A, 582, A63
Cresci, G., Tozzi, G., Perna, M., et al. 2023, A&A, 672, A128
Das, V., Crenshaw, D. M., Kraemer, S. B., & Deo, R. P. 2006, AJ, 132, 620
Di Matteo, T., Springel, V., & Hernquist, L. 2005, Nature, 433, 604
Dors, O. L., Cardaci, M. V., Hägele, G. F., et al. 2015, MNRAS, 453, 4102
Dors, Jr., O. L. & Copetti, M. V. F. 2006, A&A, 452, 473
Esparza-Arredondo, D., Ramos Almeida, C., Audibert, A., et al. 2025, A&A, 693, A174
Fabian, A. C. 2012, ARA&A, 50, 455
Farcy, M., Hirschmann, M., Somerville, R. S., et al. 2025, MNRAS, 543, 967
Faucher-Giguère, C.-A. & Quataert, E. 2012, MNRAS, 425, 605
Feltre, A., Gruppioni, C., Marchetti, L., et al. 2023, A&A, 675, A74
Ferland, G. J., Korista, K. T., Verner, D. A., et al. 1998, PASP, 110, 761
Feruglio, C., Fabbiano, G., Bischetti, M., et al. 2020, ApJ, 890, 29
Fiore, F., Feruglio, C., Shankar, F., et al. 2017, A&A, 601, A143
Fluetsch, A., Maiolino, R., Carniani, S., et al. 2019, MNRAS, 483, 4586
Gallimore, J. F., Baum, S. A., O'Dea, C. P., & Pedlar, A. 1996, ApJ, 458, 136
García-Bernete, I., Alonso-Herrero, A., Rigopoulou, D., et al. 2024, A&A, 681, L7
García-Burillo, S., Combes, F., Ramos Almeida, C., et al. 2019, A&A, 632, A61
García-Burillo, S., Combes, F., Usero, A., et al. 2014, A&A, 567, A125
Girdhar, A., Harrison, C. M., Mainieri, V., et al. 2022, MNRAS, 512, 1608
GRAVITY Collaboration, Pfuhl, O., Davies, R., et al. 2020, A&A, 634, A1
Gutkin, J., Charlot, S., & Bruzual, G. 2016, MNRAS, 462, 1757
Harrison, C. M., Alexander, D. M., Mullaney, J. R., & Swinbank, A. M. 2014, MNRAS, 441, 3306
Harrison, C. M., Costa, T., Tadhunter, C. N., et al. 2018, Nature Astronomy, 2, 198
Harrison, C. M. & Ramos Almeida, C. 2024, Galaxies, 12, 17
Hatziminaoglou, E., Zwaan, M., Andreani, P., et al. 2015, The Messenger, 162, 24
Hermosa Muñoz, L., Alonso-Herrero, A., Labiano, A., et al. 2025, A&A, 693, A321
Holden, L. R. & Tadhunter, C. N. 2023, MNRAS, 524, 886
Impellizzeri, C. M. V., Gallimore, J. F., Baum, S. A., et al. 2019, ApJ, 884, L28
Jensen, J. J., Hönig, S. F., Rakshit, S., et al. 2017, MNRAS, 470, 3071
Kakkad, D., Groves, B., Dopita, M., et al. 2018, A&A, 618, A6
Kewley, L. J., Heisler, C. A., Dopita, M. A., & Lumsden, S. 2001, ApJS, 132, 37
King, A. & Pounds, K. 2015, ARA&A, 53, 115
Kormendy, J. & Ho, L. C. 2013, ARA&A, 51, 511
Kristensen, L. E., Godard, B., Guillard, P., Gusdorf, A., & Pineau des Forêts, G. 2023, A&A, 675, A86
Labiano, A., Argyriou, I., Álvarez-Márquez, J., et al. 2021, A&A, 656, A57
Lodato, G. & Bertin, G. 2003, A&A, 398, 517
Longinotti, A. L., Salomé, Q., Feruglio, C., et al. 2023, MNRAS, 521, 2134
López, I. E., Bertola, E., Reynaldi, V., et al. 2025, A&A, 704, A88
Luridiana, V., Morisset, C., & Shaw, R. A. 2015, A&A, 573, A42
Marasco, A., Cresci, G., Nardini, E., et al. 2020, A&A, 644, A15
Marconcini, C., Feltre, A., Lamperti, I., et al. 2025a, A&A, 701, A113
Marconcini, C., Marconi, A., Cresci, G., et al. 2025b, Nature Astronomy
Marconcini, C., Marconi, A., Cresci, G., et al. 2023, A&A, 677, A58
Marconi, A., Amiri, A., Feltre, A., et al. 2024, A&A, 689, A78
Marin, F., Marinucci, A., Laurenti, M., et al. 2024, A&A, 689, A238
Markwardt, C. B. 2009, in Astronomical Society of the Pacific Conference Series, Vol. 411, Astronomical Data Analysis Software and Systems XVIII, ed. D. A. Bohlender, D. Durand, & P. Dowler, 251
May, D. & Steiner, J. E. 2017, MNRAS, 469, 994
McConnell, N. J. & Ma, C.-P. 2013, ApJ, 764, 184
Meena, B., Crenshaw, D. M., Schmitt, H. R., et al. 2023, ApJ, 943, 98
Meenakshi, M., Mukherjee, D., Wagner, A. Y., et al. 2022, MNRAS, 516, 766
Méndez-Delgado, J. E., Esteban, C., García-Rojas, J., Kreckel, K., & Peimbert, M. 2023, Nature, 618, 249
Micelotta, E. R., Jones, A. P., & Tielens, A. G. G. M. 2010, A&A, 510, A36
Mingozzi, M., Cresci, G., Venturi, G., et al. 2019, A&A, 622, A146
Monfredini, T., Quitián-Lara, H. M., Fantuzzi, F., et al. 2019, MNRAS, 488, 451
Morrison, J. E., Dicken, D., Argyriou, I., et al. 2023, PASP, 135, 075004
Mukherjee, D., Bicknell, G. V., Sutherland, R., & Wagner, A. 2016, MNRAS, 461, 967
Mukherjee, D., Bicknell, G. V., Wagner, A. Y., Sutherland, R. S., & Silk, J. 2018a, MNRAS, 479, 5544
Mukherjee, D., Wagner, A. Y., Bicknell, G. V., et al. 2018b, MNRAS, 476, 80
Müller-Sánchez, F., Prieto, M. A., Hicks, E. K. S., et al. 2011, ApJ, 739, 69
Mutie, I. M., Williams-Baldwin, D., Beswick, R. J., et al. 2024, MNRAS, 527, 11756
Navarro, J. F., Frenk, C. S., & White, S. D. M. 1997, ApJ, 490, 493
Nicholls, D. C., Sutherland, R. S., Dopita, M. A., Kewley, L. J., & Groves, B. A. 2017, MNRAS, 466, 4403
Osterbrock, D. E. & Ferland, G. J. 2006, Astrophysics of gaseous nebulae and active galactic nuclei
Patapis, P., Argyriou, I., Law, D. R., et al. 2024, A&A, 682, A53
Perrin, M. D., Sivaramakrishnan, A., Lajoie, C.-P., et al. 2014, in Society of Photo-Optical Instrumentation Engineers (SPIE) Conference Series, Vol. 9143, Space Telescopes and Instrumentation 2014: Optical, Infrared, and Millimeter Wave, ed. J. M. Oschmann, Jr., M. Clampin, G. G. Fazio, & H. A. MacEwen, 91433X
Pillepich, A., Springel, V., Nelson, D., et al. 2018, MNRAS, 473, 4077
Ramos Almeida, C., García-Bernete, I., Pereira-Santaella, M., et al. 2025, A&A, 698, A194
Revalski, M., Crenshaw, D. M., Rafelski, M., et al. 2022, ApJ, 930, 14
Revalski, M., Meena, B., Martinez, F., et al. 2021, ApJ, 910, 139

Rieke, G. H., Ressler, M. E., Morrison, J. E., et al. 2015, PASP, 127, 665
Riffel, R. A., Colina, L., Costa-Souza, J. H., et al. 2025, arXiv e-prints, arXiv:2510.02517
Riffel, R. A., Storchi-Bergmann, T., & Riffel, R. 2015, MNRAS, 451, 3587
Riffel, R. A., Storchi-Bergmann, T., Riffel, R., et al. 2023, MNRAS, 521, 1832
Schawinski, K., Thomas, D., Sarzi, M., et al. 2007, MNRAS, 382, 1415
Schinnerer, E., Eckart, A., Tacconi, L. J., Genzel, R., & Downes, D. 2000, ApJ, 533, 850
Schutte, Z., Reines, A. E., & Greene, J. E. 2019, ApJ, 887, 245
Shimizu, T. T., Davies, R. I., Lutz, D., et al. 2019, MNRAS, 490, 5860
Spoon, H. W. W., Hernán-Caballero, A., Rupke, D., et al. 2022, ApJS, 259, 37
Tanner, R. & Weaver, K. A. 2022, AJ, 163, 134
Ulivi, L., Venturi, G., Cresci, G., et al. 2024, A&A, 685, A122
Vazdekis, A., Sánchez-Blázquez, P., Falcón-Barroso, J., et al. 2010, MNRAS, 404, 1639
Veilleux, S., Maiolino, R., Bolatto, A. D., & Aalto, S. 2020, A&A Rev., 28, 2
Venturi, G., Cresci, G., Marconi, A., et al. 2021, A&A, 648, A17
Venturi, G., Nardini, E., Marconi, A., et al. 2018, A&A, 619, A74
Wagner, A. Y., Bicknell, G. V., & Umemura, M. 2012, ApJ, 757, 136
Ward, S. R., Costa, T., Harrison, C. M., & Mainieri, V. 2024, MNRAS, 533, 1733
Wells, M., Pel, J. W., Glasse, A., et al. 2015, PASP, 127, 646
Wilson, A. S. & Ulvestad, J. S. 1983, ApJ, 275, 8
Wootten, A. & Thompson, A. R. 2009, IEEE Proceedings, 97, 1463
Zhang, L., Packham, C., Hicks, E. K. S., et al. 2024, ApJ, 974, 195
Zhang, Y., Viti, S., García-Burillo, S., & Huang, K. Y. 2025, A&A, 698, A17
Zubovas, K., Bialopetravičius, J., & Kazlauskaitė, M. 2022, MNRAS, 515, 1705
Zubovas, K. & King, A. 2012, ApJ, 745, L34
Zubovas, K. & Tartėnas, M. 2025, arXiv e-prints, arXiv:2510.14667

[1] Dipartimento di Fisica e Astronomia, Università degli Studi di Firenze, Via G. Sansone 1,I-50019, Sesto Fiorentino, Firenze, Italy
[2] INAF - Osservatorio Astrofisico di Arcetri, Largo E. Fermi 5, I-50125, Firenze, Italy
[3] Center for Physical Sciences and Technology, Saulėtekio al. 3, Vilnius LT-10257, Lithuania
[4] Centro de Astrobiología (CAB), CSIC-INTA, Ctra. de Ajalvir km 4, Torrejón de Ardoz, E-28850, Madrid, Spain
[5] Instituto de Radioastronomía y Astrofísica, Universidad Nacional Autónoma de México, Morelia, Michoacán 58089, Mexico
[6] European Southern Observatory, Karl-Schwarzschild-Str. 2, D-85487 Garching, Germany
[7] Instituto de Astrofísica de Canarias, 38205 La Laguna, Tenerife, Spain
[8] Departamento de Astrofísica, Universidad de La Laguna, 38206 La Laguna, Tenerife, Spain
[9] INAF - Osservatorio di Astrofisica e Scienza dello Spazio di Bologna, via Gobetti 93/3, 40129, Bologna, Italy
[10] AURA for ESA, Space Telescope Science Institute, 3700 San Martin Drive, Baltimore, MD 21218, USA
[11] INAF – Osservatorio Astronomico di Trieste, Via G. Tiepolo 11, 34143 Trieste, Italy
[12] IFPU – Institute for Fundamental Physics of the Universe, Via Beirut 2, 34151 Trieste, Italy
[13] Centro de Estudios de Física del Cosmos de Aragón (CEFCA), Plaza San Juan 1, 44001 Teruel, Spain
[14] Max-Planck-Institut für extraterrestrische Physik (MPE), Gießenbachstraße 1, 85748 Garching, Germany
[15] Observatorio Astronómico Nacional, C Alfonso XII 3, 28014 Madrid, Spain
[16] Dipartimento di Fisica e Astronomia “Augusto Righi", Università degli Studi di Bologna, Via Gobetti 93/2, 40129 Bologna, Italy
[17] Scuola Normale Superiore, Piazza dei Cavalieri 7, I-56126 Pisa, Italy

Appendix A: Data reduction

In this Appendix we present an overview of the data reduction we carried out for the MIRI/MRS, MUSE, and ALMA data.

Appendix A.1: MIRI/MRS data reduction

We downloaded the uncalibrated science and background observations through the MAST portal. The data reduction process was done using the JWST Science Calibration Pipeline (Bushouse et al. 2022) version 1.16.0. We applied all the three stages of the pipeline processing, which include `CALWEBB_DETECTOR1`, `CALWEBB_SPEC2`, and `CALWEBB_SPEC3` (see Morrison et al. 2023; Patapis et al. 2024). Additional fringe corrections were made in both the stage 2 and stage 3 products using the standard pipeline code. We adopted the FASTR1 readout pattern to optimize the dynamic range expected in the observations. Because our source is extended, we linked the observation to a dedicated background with the same observational parameters in all three grating settings allowing us to perform a pixel-by-pixel background subtraction. The result of the data reduction pipeline are 12 flux-calibrated data-cubes oriented with the world coordinates, and which span progressively larger FoV, from 3.2×3.7 in Channel 1 to 6.6×7.7 in Channel 4. Moreover, from Channel 1 to Channel 4, data-cubes have a progressively coarser spaxel sampling, i.e. 0.13, 0.17, 0.2, and 0.35 $''$/pxl. For details on the data reduction steps we refer to Marconcini et al. (2025a).

Appendix A.2: MUSE data reduction

We retrieved the data from the ESO archive [3], reduced with the standard MUSE pipeline (v1.6)[4]. The final data-cube consist of 281×281 spaxels, with a spatial sampling of 0.2$''$/pixel, covering the spectral range 4750–9350 Å, thus tracing the rest-frame optical wavelength range. The MUSE spectral resolution span from 1750 at 4650 Å to 3750 at 9300 Å. With its large FoV of $1' \times 1'$the observations cover a portion of 3×3 kpc at the distance of NGC 1068.

Appendix A.3: ALMA data reduction

We requested the calibrated measurement sets from the European ALMA Regional Centre (ARC; Hatziminaoglou et al. 2015). To reduce and analyse the data we used the Common Astronomy Software Applications (CASA) package version v5.6.1 (CASA Team et al. 2022). To obtain the CO(2-1) data cube, we subtracted a constant continuum level estimated from the emission line free channels in the *uv* plane[5]. The data were cleaned using the CASA task TCLEAN using a BRIGGS weighting scheme with ROBUST = 0.5, to achieve a $\sim$ 19 pc resolution (beam size FWHM $0.33'' \times 0.37''$, beam PA = 1°). The final reduced data cube has a spectral channel width of $\sim$ 5 km s^{-1}, a pixel size of 90 mas, and an rms of 0.94 mJy/beam per channel.

Appendix B: Emission line fitting procedure

To investigate the multi-phase gas properties in NGC 1068 we used an emission line fitting routine which we tailored to each instrument, e.g. taking into account the wavelength dependent spectral resolution, spectral channel width and spatial PSF of each instrument.

To analyze the MUSE data we followed the spectroscopic routine outlined in Marasco et al. (2020). First, we performed a Voronoi tessellation (Cappellari & Copin 2003) in order to achieve an average signal-to-noise (S/N) ratio of 30 per wavelength channel on the continuum. Then, we used the pPXF (penalized pixel fitting, Cappellari & Emsellem 2004) code on the binned spaxels to simultaneously fit the emission lines and stellar features in the observed spectral range 4750-9000 Å. In particular, to fit the stellar continuum we used a linear combination of synthetic single stellar population (SSP) templates from Vazdekis et al. (2010), for single-age and metallicity stellar populations, which we convolved with the MUSE spectral resolution, and then shifted, broadened, and combined with a first degree additive polynomial to reproduce the observed features. Additionally, to properly fit the stellar features underlying Balmer emission lines we fitted the SSP templates together with the main gas emission lines, using up to four Gaussian components to account for the complex, asymmetric line profiles in the circumnuclear region of NGC 1068. We then subtracted the best-fit continuum in each bin and obtained a continuum-subtracted model cube which we spatially smoothed using a Gaussian kernel with σ = 1 spaxel (i.e. 0.2$''$) to conserve the native MUSE spatial resolution. Then, we focused on the smoothed continuum-subtracted data cube to perform a detailed emission line fitting. In particular, we fitted the emission lines falling within the mentioned spectral range using the MPFIT fitting tool (Markwardt 2009) and up to four Gaussian components, tying the velocity and velocity dispersion of each component. Moreover, we fixed the flux ratio between the two lines in each doublet, i.e. [O III]$\lambda\lambda$4959,5007, and [N II]$\lambda\lambda$6549,6584 as given by the Einstein coefficients of the two transitions (Osterbrock & Ferland 2006). The optimal number of Gaussian components is decided based on the χ^2 minimization and a Kolmogorov-Smirnov test. As a result, we obtain an emission-line model cube for the following optical transitions: Hα, Hβ, Hγ, [O III]$\lambda\lambda$4959,5007, [N II]$\lambda\lambda$6549,6584, [S II]$\lambda\lambda$6716,6731.

To analyze the MIRI/MRS data-cubes we followed a similar approach. In particular, we focused on a spectral band encompassing a velocity range of $\pm$ 2500 km s^{-1} around each emission line in each channel and simultaneously fitted a first degree polynomial and up to four Gaussian components using the MPFIT fitting tool to reproduce the continuum slope and the asymmetric line profile in each spaxel, respectively. Similarly to the outcome of the MUSE spectroscopic routine, the final results of this procedure is a dedicated model cube for each Gaussian component and one for the total best-fit profile, for each emission line. Tab. D.1 lists the fluxes and uncertainties of all the fitted emission lines, extracted from the FoV of Ch1.

To analyze the spatially resolved properties of the cold molecular gas in NGC 1068 we exploited the CO (2-1) transition observed in the ALMA band 6 data. Here, at variance with the routine described for the analysis of MRS data-cubes, the continuum was already subtracted in the uv-plane during the data reduction. Therefore, we carried out a detailed spaxel-by-spaxel multi-Gaussian fit to the CO (2-1) transition. Similarly to other transitions, we noticed that multiple Gaussians are needed to reproduce the CO (2-1) profile across the ALMA FoV.

[3] https://archive.eso.org/cms.html

[4] https://data.aip.de/data/musepipeline/v1.6/

[5] The continuum was modeled using the line free spectral channels in the spectral windows [226.91, 228.79] GHz and [229.29, 231.27] GHz.

Appendix C: Kinematic modeling with MOKA^{3D}

Figure C.1 shows the comparison between the observed moment maps and the best-fit moment maps inferred by our multi-cloud kinematic model MOKA^{3D} for the [O III] (top panels) and [O IV] (bottom panels) emission from MUSE and MIRI data, respectively. The kinematic model free parameters are the outflow radial velocity and inclination with respect to the LOS in each shell. For details on the modeling strategy and the best-fit parameters see Sect. 3.4.1, Tab. 1 and Fig. 7.

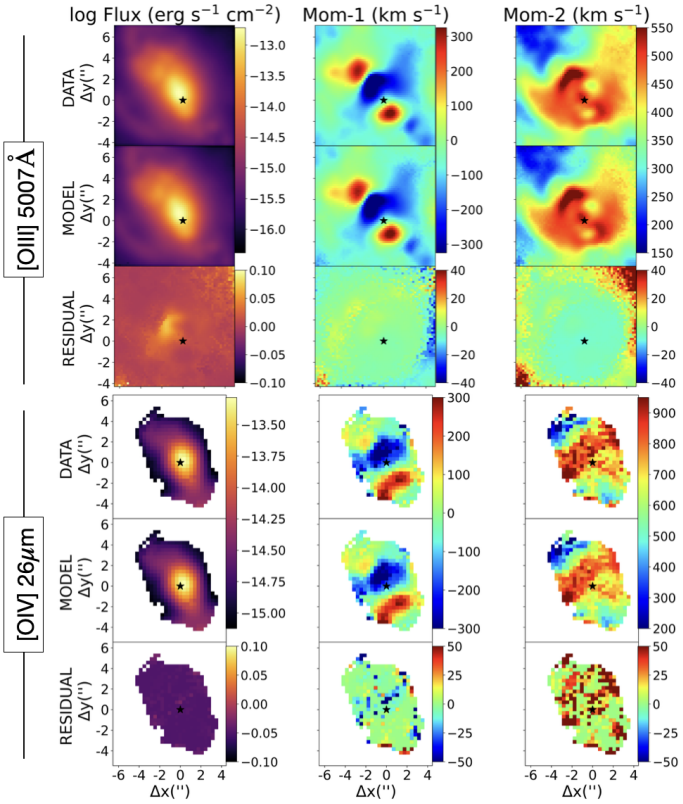

Fig. C.1. MOKA^{3D} best-fit model for the ionized outflow traced by the [O III] (top panels) and [O IV] (bottom panels) emission lines from MUSE and MIRI MRS, respectively. Panels show the observed (top), best-fit (center) and residual (bottom) moment maps derived with MOKA^{3D}. The residual maps are obtained by subtracting the model from the observed moment maps. The star marks the position of the nucleus.

As an example, Fig. C.2 shows the 3D distribution of the [O III]-traced ionized gas clouds within the bi-conical outflow model of NGC 1068 computed with MOKA^{3D}, with the cloud size being proportional to the intrinsic cloud luminosity.

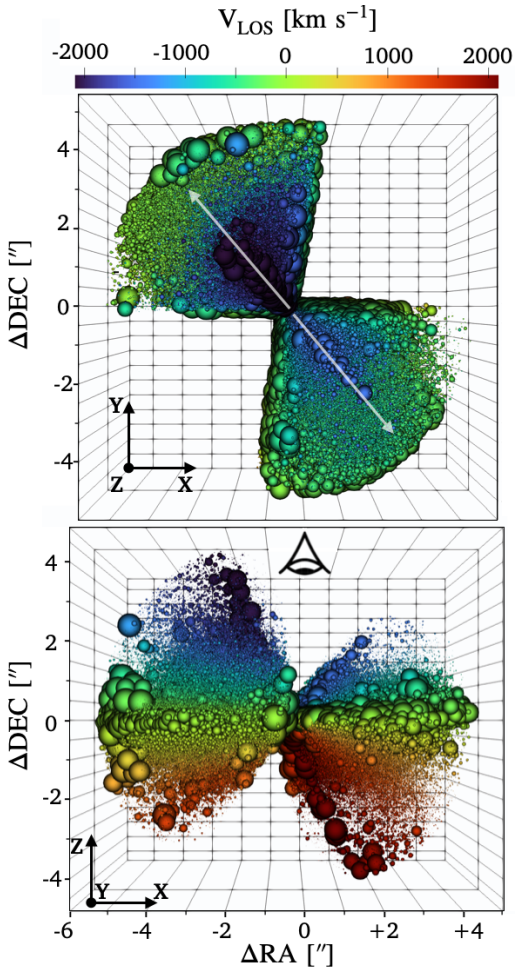

Fig. C.2. 3D reconstruction of the MOKA^{3D} best-fit model of the ionized outflow traced by [O IV] emission obtained with the parameter presented in Sec. 3.4.1. Gas clouds are color-coded by their velocity along the line-of-sight and their size scales with the intrinsic flux of each cloud. The X-Y plane represents the plane of the sky, and the Z axis is the LOS. Top panel: view along the LOS. Bottom panel: view along the plane of the sky, with the observer positioned along the Z-axis. The gray arrow indicates the direction of the conical outflow axis.

Appendix D: HOMERUN set-up and AGN+SF fit

In this section we present the HOMERUN model set-up that we adopted to obtain the best-fit presented in Sect. 3.4.3. For a comprehensive overview of the multi-clouds model see Marconi et al. (2024).

Appendix D.1: HOMERUN modeling set-up

We first define a wide grid of CLOUDY models including n_H and U for a fixed ionizing spectrum (S_ν), gas-phase oxygen abundance (A_O), and elemental abundance ratios (Z). Then, HOMERUN runs a Non-Negative Least Squares fit assigning positive weights to each cloud to finally infer the best-fitting multi-cloud model by combining individual single-cloud templates. In doing so, we imposed no regularization, thus allowing for full flexibility to the weight assignment. The process is repeated across all available grids, spanning different ionizing continua, metallicities, and abundance scalings. The optimal solution is identified as the one minimizing the loss function $\mathscr{L}_{min}(S_\nu, A_O, Z)$, which quantifies the deviation between model predictions and observed emission-line fluxes. This loss function is effectively a reduced χ^2 statistic, so values $\lesssim 1$ indicate a statistically good fit (see e.g. Marconi et al. 2024, Moreschini et al. in prep.).

When exploring different metallicities, elemental abundances were scaled from the solar photospheric values of Asplund et al. (2021), except for carbon and nitrogen, which were rescaled following the prescriptions of Nicholls et al. (2017), with an additional +0.2 dex offset applied to nitrogen. During the fit, all elemental abundances except oxygen were allowed to vary from their initial values. Since the H$_{mod,2}$ component was assumed to be dust-free while the H$_{mod,1}$ component includes dust,

refractory elements are allowed to have different scaling factors due to depletion on dust, whereas non-refractory elements share the same scaling factor in both components. Similarly as done in Ceci et al. (2025), we modeled the AGN ionizing radiation field as a power law with UV slope α_{UV} = -0.5, exponential cut-off exp(-hν/k T_{Max}) and the X-ray component slope of α_X=-1.0, with the X-ray component being linked to the UV through α_{OX}. We computed models with combinations of log(T_{Max}/K) = 4.0, 4.5, 5.0, 5.5, 6.0, 6.5, 7.0 and α_{OX} = -1.2, -1.5, -1.8. As a result, the best-fit provides log(T_{Max}/K) = 6.0 for both $H_{mod,1}$ and $H_{mod,2}$ grid of AGN models.

Appendix D.2: Combination of AGN and SF models

In Sect. 3.4.3 we presented various evidences supporting the use of pure AGN models to fit the observed multi-wavelength set of emission lines. For completeness, we also performed a fit of the observed features adopting a combination of dust-free gas ionized by the AGN and emission from dusty nebulae around H II regions, with the latter accounting for possible star formation contribution. We run the HOMERUN fit over the same n_H–U grid as for the pure-AGN fit and found a minimum at $\mathscr{L}$ = 1.58, i.e. $\sim$ 4 times larger compared to the pure-AGN fit, with emission lines being reproduced within a $\sim$ 40% accuracy. Moreover, adopting a combination of AGN+SF models we found luminosity-to-mass conversion factors (see Eq. 1) of $C_{AGN} = 5.9 \times 10^5$ $M_\odot/(10^{40}$ erg/s) and $C_{SF} = 6.4 \times 10^3$ $M_\odot/(10^{40}$ erg/s) together with an 100% of fraction of the O species produced by the AGN component, thus not affecting the estimated outflow energetic properties listed in Tab. 2. These results, combined with no evidence of ordered ionized gas kinematic and no hint of star formation ionization either from Mid-IR or optical diagnostic diagrams further corroborate the pure AGN ionization scenario.

Appendix E: Set-up of the energy-driven model

The numerical scheme MAGNOFIT used in Sect. 3.4.2 is a numerical integrator tracking the evolution of the outflow radius and velocity in a spherically symmetric mass distribution whose components have analytically-expressible mass profiles. The details of the equation of motion are given in the Appendix of Zubovas et al. (2022) and are a generalization of the energy-driven outflow equation of motion as presented in King & Pounds (2015). Recently, this code was used to explain the acceleration of outflows in a sample of galaxies with spatially-resolved ionized gas kinematics (Zubovas & Tartėnas 2025). Such behavior can be explained with a two-component model, with a gas-rich bulge and a gas-poor halo outside it, with the outflow accelerating once the edge of the bulge is reached. The more complex kinematics of NGC 1068, with an initial acceleration, followed by a slowdown phase beyond which the gas begins accelerating once again, requires a three-component model.

We determined the model parameters by iterative fitting. First, we fixed the velocity dispersion at $\sigma = 150$ km s^{-1} and the SMBH mass at 4×10^7 $M_\odot$, which is the appropriate mass following the $M - \sigma$ relation from McConnell & Ma (2013). We stress that the precise value of M_{BH} does not affect the final result, because the SMBH gravity is only relevant in the inner unresolved regions. Then, we determined the approximate bulge mass and radius by fitting a two-component model as in Zubovas & Tartėnas (2025), with an isothermal bulge density profile. We found $M_b = 2.9 \times 10^9$ $M_\odot$, around a factor 3 lower than given by the BH-bulge mass relation (Schutte et al. 2019), but well within the scatter of the data. As a result, we infer a bulge gas fraction of $f_g = 6.8 \times 10^{-3}$ with a bulge radius of 0.39 kpc. The region outside the bulge is modeled with an NFW halo with a total mass $M_h = 4 \times 10^{12}$ $M_\odot$ and a gas fraction $f_{g,h} = 10^{-3}$. Next, we replaced the bulge with a two-component structure with power-law density profiles, keeping the total mass and gas fraction the same. We then fit the values of the two power-law slopes, the transition radius and the relative mass contribution of each component. We did this iteratively by minimizing the chi-squared difference between the calculated and observed velocity values at the positions of the observed data points. The best-fitting model has a transition radius at $R_{tr} = 0.14$ kpc, and the outer component contains $\sim$ 80% of the total bulge mass. The two power-law slopes are given in Figure 7.

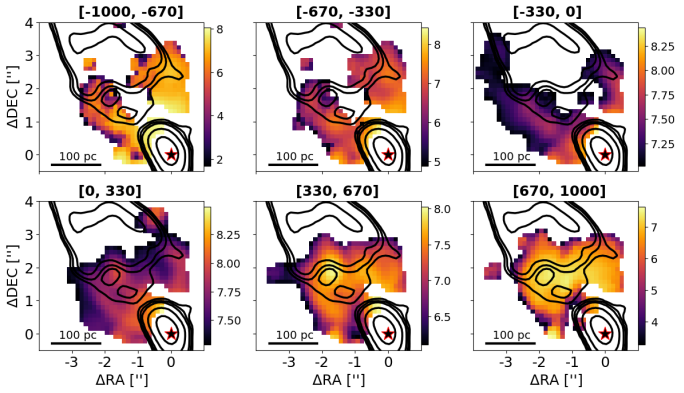

Fig. F.1. Channel maps of [Ar II]6.98μm from MIRI data in unit of 10^{-20} erg/s/cm^{-2}. Velocity bins are indicated at the top of every panel in kilometers per second and are computed relative to the same systemic velocity. Black contours represent the same VLA contours of Fig. 1 and the black star mark the X-ray inferred nucleus position.

Appendix F: Tracing the bow-shock with Mid-IR transitions

In this appendix we exploit the ionic fine-structure lines [Ar II]6.98μm in MIRI MRS Ch2 to spatially trace shocked gas and the presence of bow-shocks in the circumnuclear region of NGC 1068. Such transition originates in low-to-moderately ionized gas (IP = 16 eV) which is efficiently excited by shocks and is only mildly sensitive to the hardest photoionizing continuum, making it dominant in collisional heated regions of shocks. Therefore, such transition provide a reliable probe of the spatial extent and location of bow shocks in the inner few hundreds of parsec, likely tracing the radio bow-shocks morphology detected by Mutie et al. (2024).

Figure F.1 shows velocity channel maps of [Ar II]6.98μm with VLA radio contours overlapped. As expected, we notice that the [Ar II] transition nicely match the observed morphology of the radio emission, with blue-shifted maps clearly showing two arms extending from the nuclear region and surrounding the edges of the northern radio lobe up to the MIRI/MRS Ch2 FoV coverage. On the other hand, red-shifted channel maps show clumpy peaks of the [Ar II] emission towards the lower edge of the radio lobe highlighted by VLA contours, likely where the radio-jet start impacting the host galaxy. Overall, the [Ar II] emission traces the edge of the radio-jet, where bow-shocks originate due to the impact with the ambient ISM, and co-spatially with the peaks of H_2 content.

Table D.1. Mid-IR and optical emission line fluxes in units of 10^{-14} erg s^{-1} cm^{-2} used for the HOMERUN fit presented in Sect. 3.4.3.

Optical lines			Mid-IR lines		
Line	Wavelength [Å]	Flux [10^{-14} erg s^{-1} cm^{-2}]	Line	Wavelength [μm]	Flux [10^{-14} erg s^{-1} cm^{-2}]
Hβ	4861	79.1±0.6	H_2S(8)	5.0529	0.2*
[O III]	5007	863±1	Fe II	5.340	9.8±0.9
[N I]	5198	7.4±0.1	Fe VIII	5.447	6.6±0.3
[Fe XIV]	5303	9.7*	[Mg VII]	5.503	9.6±0.3
He II	5411	2.4±0.3	H_2S(7)	5.511	0.99±0.07
[Fe VII]	5721	9.5±0.1	[Mg V]	5.607	27.1±0.9
[N II]	5755	9.4±0.1	H_2S(6)	6.109	1.7±0.2
He I	5876	104±1	[Ni II]	6.634	9.6*
[Fe VII]	6087	23±2	Fe II	6.710	3.4*
[O I]	6300	36±2	H_2S(5)	6.909	8.5±0.3
[S III]	6312	11±2	[Ar II]	6.985	130±7
[Fe X]	6375	6.5±0.7	[Na III]	7.315	39±1
Hα	6563	241±12	Pfα	7.457	0.07*
[N II]	6584	432±27	[Ne VI]	7.6524	715±30
[S II]	6717	58±2	Fe VII	7.8145	15±6
[S II]	6731	52±3	[Ar V]	7.902	24±1
[Ar V]	7006	5.3±0.7	H_2S(4)	8.026	3.5±0.2
He I blend	7065	7.2±0.4	[Na VI]	8.608	6.7*
[Ar III]	7136	36±1	[Ar III]	8.991	225±11
[O II] blend	7323	14±4	Fe VII	9.527	47±3
[O II] blend	7332	9.6±0.9	H_2S(3)	9.665	7.1±0.3
[Ni II]	7378	4.5±0.8	[S IV]	10.511	670±66
[Ar III]	7751	8.2±0.7	H_2S(2)	12.279	3.439±0.6
[Fe XI]	7892	3.9±0.4	[Ne II]	12.814	636±70
[Cl II]	8579	4.7±0.5	[Ar V]	13.102	43±4
[Fe II]	8617	7.2±0.8	[Ne V]	14.322	970±70
[S III]	9068	98±1	[Ne III]	15.555	1430±50
			H_2S(1)	17.035	4.4±0.5
			Fe II	17.931	75±6
			[S III]	18.713	330±18
			Fe VI	19.553	15*
			Fe III	22.925	23*
			[Ne V]	24.318	423±24
			[O IV]	25.890	1130±190
			Fe II	25.988	106±9

Notes. From left to right: Line name, rest-frame wavelength, line fluxes and uncertainties. Fluxes are extracted from the FoV of MIRI/MRS Ch1 and the Mid-IR fluxes are corrected for the appropriate flux scaling factor among different bands. The values marked with an asterisk represent a 3σ upper limit.

Appendix G: Rotation curve and dynamical mass fit

In this section we present the result of the kinematic fit of the ordered motions within the galactic disc of NGC 1068 exploiting a multi-shell fit with MOKA^{3D}of MUSE data. In particular, we fit a circular thin disc with inner and outer radius of 4-50″ (∼ 0.3-3.4 kpc), divided in 46 concentric annuli of fixed width of 1″ (70 pc), comparable to the MUSE FWHM. Due to the outshining outflow emission within the central 4″ we could not securely identify the narrow [O III] component in this region and therefore set the inner disc radius to 4″ scale. The fit provides the inclination and circular velocity in each shell, similarly to the procedure carried out for the outflow fit in Sect. 3.4.1. As a result we find that the disc is inclined of 57° ± 3° with respect to the LOS, consistently with previous analysis (Bland-Hawthorn et al. 1997). The circular velocity as a function of the radius is shown in Fig. G.1, showing peak velocities of ∼ 250 km s^{-1}, consistently with Meena et al. (2023). We derived the dynamical mass profile in NGC 1068 from the deprojected circular velocities in each shell assuming circular motion in a spherically symmetric potential:

$$M(<R) = \frac{V_{\rm circ}(R)^2 R}{G} \tag{G.1}$$

where R is the galactocentric radius in kiloparsecs and G is the gravitational constant. We computed the uncertainties on $M(<R)$ propagating the uncertainties of the circular velocities and inclination. This procedure provides a direct estimate of the enclosed dynamical mass as a function of radius, under the assumption that the gas trace circular motion in the plane of the disc and that non-circular motions are negligible. The resulting mass within 50″ is $M(<R) = 2.05 \pm 0.2 \times 10^{10}$ M$_\odot$. Our result are fully consistent with the enclosed mass inferred from large-scale H I and CO rotation curves (e.g., Schinnerer et al. 2000), which reach a few $\times 10^{10} M_\odot$ within several kiloparsecs.

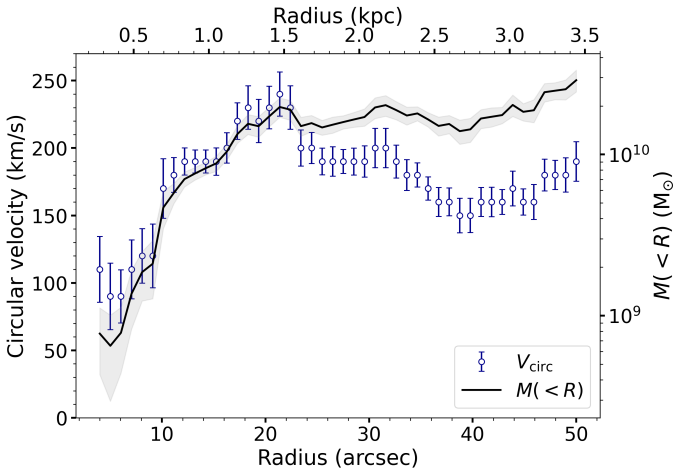

Fig. G.1. NGC 1068 rotation curve inferred with MOKA^{3D} using the narrow component of the [O III] emission line from MUSE data (blue) and dynamical mass profile with its uncertainty (solid black). For details see App. G.

Appendix H: Standard approach to estimate the ionized gas mass

Here we provide a brief overview of the gas mass estimate for the [O III] and [O IV] emission lines, following the same approach as in Ceci et al. (2025) and extending it to the [O IV] gas. The line luminosity of the species $[O\,X]$ can be written as:

$$L_{[\mathrm{O\,X}]} = \int_V f\, n_e\, n\left(O^{X+}\right)\, \gamma_{[\mathrm{O\,X}]}(n_e, T_e) dV \tag{H.1}$$

with f the filling factor, V the volume occupied by the outflowing ionized gas, n_e the electron density, $n(O^{X+})$ the density of O^{X+} ions, and $\gamma_{[\mathrm{O}]}(n_e, T_e)$ the line emissivity with X being 2 ([O III]) or 3 ([O IV]). We can write $n(O^{X+})$ as:

$$n\left(O^{X+}\right) = \left[\frac{n\left(O^{X+}\right)}{n(O)}\right]\left[\frac{n(O)}{n(H)}\right]\left[\frac{n(H)}{n_e}\right] n_e.$$

Assuming $n(O^{X+}) \approx n(O)$, $n_e \approx 1.2\, n(H)$ (i.e. a 10% number density of He atoms with respect to H atoms), and a solar abundance of [O/H] $\sim$ 8.69 (Asplund et al. 2009), we obtain $n(O^{X+}) \sim 4.08 \times 10^{-4} n_e$. Then, assuming a temperature of $T_e \simeq 10^4$K, an electron density of $n_e = 10^{3.5\pm0.4}$ cm^{-3} ($10^{3.9\pm0.3}$ cm^{-3}) from the Sulfur (Neon) emission lines we used the PyNeb tool (Luridiana et al. 2015) to estimate a line emissivity of $\gamma_{[\mathrm{O\,III}]} = 3.67 \times 10^{-21}$ erg s^{-1} cm^3 ($\gamma_{[\mathrm{O\,IV}]} = 2.3 \times 10^{-21}$ erg s^{-1} cm^3). Assuming a constant electron density in the outflow volume, we can write Eq. H.1 as:

$$L_{[\mathrm{O\,X}]} = 4.08 \times 10^{-4} f\, n_e^2\, \gamma_{[\mathrm{O\,X}]}\, V, \tag{H.2}$$

The mass of the gas can be written as:

$$M = \int_V f\, \bar{m}\, n(H) dV \simeq \int_V f\, m_p\, n_e dV, \tag{H.3}$$

where $\bar{m}$ = 1.27 m_p assuming a 10% fraction of He atoms, and we have taken into account that:

$$\bar{m}\, n(H) = \bar{m}\left[\frac{n(H)}{n_e}\right] n_e = 1.27\, m_p\, (1.2)^{-1}\, n_e \approx m_p\, n_e, \tag{H.4}$$

therefore, $M \approx f\, m_p\, n_e\, V$. Combining this latter with Equation H.2, we finally get:

$$\mathrm{M_{out}} = \beta \left(\frac{\mathrm{L_{[OX]}}}{10^{36}\,\mathrm{erg\,s^{-1}}}\right)\left(\frac{\mathrm{n_e}}{200\,\mathrm{cm^{-3}}}\right)^{-1} \mathrm{M_\odot}. \tag{H.5}$$

with β = 2.94 and 1.44, for [O III]λ5007 and [O IV] gas masses, respectively.